

UC San Diego

UC San Diego Previously Published Works

Title

Elemental Mixing State of Aerosol Particles Collected in Central Amazonia during GoAmazon2014/15

Permalink

<https://escholarship.org/uc/item/3x66j5vf>

Journal

Atmosphere, 8(9)

ISSN

0004-6973

Authors

Fraund, Matthew

Pham, Don

Bonanno, Daniel

et al.

Publication Date

2017

DOI

10.3390/atmos8090173

Peer reviewed

1 Article

2 Elemental Mixing State of Aerosol Particles Collected in 3 Central Amazonia During GoAmazon2014/15

4 Matthew Fraund¹, Don Q. Pham¹, Daniel Bonanno¹, Tristan H. Harder^{2,5†}, Bingbing Wang^{3,‡}, Joel
5 Brito^{6,*}, Suzane S. de Sá⁷, Samara Carbone⁶, Swarup China³, Paulo Artaxo⁶, Scot T. Martin⁷,
6 Christopher Pöhlker⁴, Meinrat O. Andreae^{4,8}, Alexander Laskin^{3,®}, Mary K. Gilles², Ryan C. Moffet^{1*}

7 ¹ University of the Pacific (UoP)

8 ² Lawrence Berkeley National Laboratory (LBNL)

9 ³ Pacific Northwest National Laboratory (PNNL)

10 ⁴ Max Planck Institute for Chemistry (MPIC)

11 ⁵ University of California, Berkeley

12 ⁶ University of Sao Paulo, Brazil (USP)

13 ⁷ Harvard University

14 ⁸ Scripps Institution of Oceanography, University of California, San Diego

15 † present address: Physikalisches Institut, Universität Würzburg, Am Hubland, 97074 Würzburg, Germany

16 ‡ present address: State Key Laboratory of Marine Environmental Science, College of Ocean and Earth Sciences,
17 Xiamen University, Xiamen, China

18 [®] present address: Purdue University (PU)

19 ^{*} present address: Laboratory for Meteorological Physics (LaMP), Université Clermont Auvergne, F-6300 Clermont-
20 Ferrand, France

21 *Correspondence: rmoffet@pacific.edu; Tel.: 209-946-2006

22 Academic Editor: name

23 Received: date; Accepted: date; Published: date

24 **Abstract:** Two complementary techniques, Scanning Transmission X-ray Microscopy/Near Edge Fine Structure
25 spectroscopy (STXM/NEXAFS) and Scanning Electron Microscopy/Energy Dispersive X-ray spectroscopy
26 (SEM/EDX), have been quantitatively combined to characterize individual atmospheric particles. This pair of
27 techniques was applied to particle samples at three sampling sites (ATTO, ZF2, and T3) in the Amazon basin as part
28 of the Observations and Modeling of the Green Ocean Amazon (GoAmazon2014/5) field campaign during the dry
29 season of 2014. The combined data was subjected to k-means clustering using mass fractions of the following
30 elements: C, N, O, Na, Mg, P, S, Cl, K, Ca, Mn, Fe, Ni, and Zn. Cluster analysis identified 12 particle types, across
31 different sampling sites and particle sizes. Samples from the remote Amazon Tall Tower Observatory (ATTO, also
32 T0a) exhibited less cluster variety and fewer anthropogenic clusters than samples collected at the sites nearer to the
33 Manaus metropolitan region, ZF2 (also T0t) or T3. Samples from the ZF2 site contained aged/anthropogenic
34 clusters not readily explained by transport from ATTO or Manaus, possibly suggesting the effects of long range
35 atmospheric transport or other local aerosol sources present during sampling. In addition, this data set allowed for
36 recently established diversity parameters to be calculated. All sample periods had high mixing state indices (χ) that
37 were >0.8 . Two individual particle diversity (D_i) populations were observed, with particles $<0.5 \mu\text{m}$ having a D_i of
38 ~ 2.4 and $>0.5 \mu\text{m}$ particles having a D_i of ~ 3.6 , which likely correspond to fresh and aged aerosols respectively. The
39 diversity parameters determined by the quantitative method presented here will serve to aid in the accurate
40 representation of aerosol mixing state, source apportionment, and aging in both less polluted and more developed
41 environments in the Amazon Basin.

42 **Keywords:** Mixing State; Amazon; Elemental Composition; Aerosol; STXM; SEM; EDX; Diversity; Aging

44 1. Introduction:

45 Atmospheric aerosols are solid or liquid particles suspended in air and are comprised of mixtures of
46 organic and/or inorganic species: organic molecules, salts, soot, minerals, and metals [1]. Aerosols have
47 highly uncertain effects on radiative forcing [2]. Aerosol forcing occurs via two mechanisms: light can be
48 scattered or absorbed directly by the aerosol particles (the “direct effect”, also aerosol-radiation
49 interactions) or indirectly through aerosol effects on cloud properties (the “indirect effect”, also aerosol-
50 cloud interactions) [3]. The latest Intergovernmental Panel on Climate Change (IPCC) report, released in
51 2013, shows that the extent of anthropogenic effects on cloud formation is currently the largest source of
52 uncertainty for predictive understanding of global anthropogenic radiative forcing [2]. Both direct and
53 indirect effects are heavily influenced by the composition of aerosols on a per-particle level [4-6]. To
54 better understand and predict the influence of industrialization, one aspect of particular interest is the
55 effect that anthropogenic emissions have on the per-particle composition of aerosols and their impacts on
56 local and global climate [2,7].

57 One underlying reason for this uncertainty is the complex manner in which aerosol composition
58 changes over time and distance through coagulation, condensation, and chemical reaction [8]. Because
59 aerosol radiative forcing and cloud formation depend on the individual particle composition, it is
60 important to know how atmospheric components are mixed within a population of aerosols. How these
61 components are mixed plays a large role in determining the manner and extent to which radiative forcing
62 is affected. For example, the coating of soot by organics can change the direct radiative forcing of those
63 aerosols by as much as a factor of 2.4 over pure soot [9-12]. Hence, in this case, it is important to know
64 whether soot and organics coexist in the same aerosol particle. How components are mixed in an aerosol
65 sample is referred to as its mixing state. This mixing state can range anywhere from an internal mixture
66 where each component is evenly distributed throughout all particles, to an external mixture where each
67 component occupies its own population of particles. Many atmospheric models assume one of these
68 extremes throughout their simulation [13-15]. Some models include a specific aspect of aerosol mixing
69 such as the mixing state of black carbon [4,16], while other, nascent, models will account for a more
70 complete mixing state [17]. Mixing state values for coated black carbon (BC) have been determined using
71 a single-particle soot photometer (SP2) based on the time delay between light scattering and soot
72 incandescence but thermodynamic properties of organic coatings must be assumed to infer coating
73 thicknesses, making the technique qualitative [18,19]. This approach also becomes less applicable if
74 inorganic dominant or non-soot containing particles are of interest. A real-time method for determining
75 aerosol mixing state index has been achieved by using single particle mass spectrometry [20], although
76 this technique is blind to detailed aerosol morphology.

77 Recently, more nuanced metrics were developed to quantify the mixing state of a population of
78 aerosols [21]. Here, Riemer and West utilize an information theoretic approach to determine specific
79 mixing states in populations of aerosols. Particle-specific mass fractions are used to calculate both bulk
80 and individual particle diversity parameters. The mixing state of a population is then calculated from the
81 ratio of individual and bulk diversities. This method of mixing state determination necessitates a mass
82 quantitative method of determining per-particle composition. Spectromicroscopy techniques are
83 uniquely suited to analyze both the morphology and the comprehensive mixing state of a population of
84 aerosols. Here, these quantitative mixing state metrics are applied to microscopy images of particle
85 samples collected in the central Amazon basin.

86 In this study, we determine the mass fractions of 14 elements on the exact same set of particles using
87 the complementary techniques of Scanning Transmission X-ray Microscopy with Near-Edge X-ray
88 Absorption Fine Structure spectroscopy (STXM/NEXAFS) and Scanning Electron Microscopy coupled
89 with Computer Controlled Energy Dispersive X-ray spectroscopy (SEM/EDX). Each technique is limited
90 in which elements it can investigate. STXM/NEXAFS is limited by the energy range of the synchrotron
91 insertion device as well as the beamtime available for sample analysis. STXM/NEXAFS has the
92 advantage of providing quantitative measurements of light, low Z (atomic number) elements (C, N, and

93 O), as well as some heavier elements with L-shell absorption edges in the same energy range (e.g., K and
94 Ca) [22,23]. Although SEM/EDX provides a faster method of per-particle spectromicroscopy, it is only
95 considered quantitative for higher Z elements ($Z > 11$, Na) [7,24,25]. These two techniques are inherently
96 complementary, with each technique providing mass information on elements that the other cannot
97 adequately probe and both providing this information on an individual particle level. Both techniques
98 have been used in tandem on microscopy samples previously [26]. In that study, O'Brien et al. used
99 STXM/NEXAFS and SEM/EDX to characterize individual particles from northern California. From this,
100 mixing state parameters were calculated; however, because STXM and SEM were conducted on different
101 particles within a given sample, separate mixing states were calculated from each technique. The current
102 work combines STXM and SEM data at the single particle level in a similar way to Piens et al., 2016 [27],
103 where both techniques were used together to determine hygroscopicity of individual particles. The per-
104 particle elemental mass fractions determined herein are used to calculate an elemental mixing state for
105 particles collected at three sampling sites.

106 Aerosol production in the Amazon basin plays an important role in global climate due to the large
107 scale of biogenic emissions from the tropical forest often mixed with pollutants from vegetation fires
108 (mostly related to deforestation and pasture burning) [28-31]. South America contributes significantly to
109 the global aerosol carbon budget; ~17% of global soot emissions are produced in Central and South
110 America combined [32]. Aerosols are also subject to long range transport and thus are of importance to
111 global models [33]. This environmentally important region of Central Amazonia contains Manaus, a city
112 with over two million people. Manaus is a large industrial manufacturing city as a consequence of its
113 free trade status since the 1960s. The juxtaposition of pristine rainforest with a large anthropogenic center
114 presents a unique circumstance for studying how native biogenic aerosols are affected by emissions from
115 an industrial city [34]. To take advantage of this unique location, the Observations and Modeling of the
116 Green Ocean Amazon (GoAmazon2014/5) field campaign was conducted from January 2014 through
117 December 2015 [35,36]. The GoAmazon campaign was developed with multiple scientific objectives, two
118 of which involve the biogenic and anthropogenic interactions studied here.

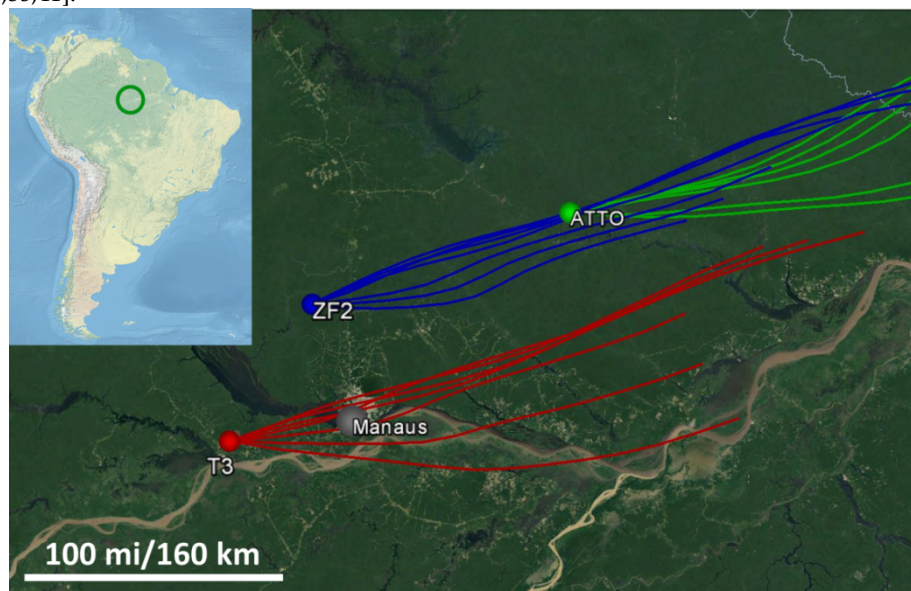
119 2. Experiments:

120 2.1. Sampling Site Description:

121 As part of the GoAmazon field campaign, two Intensive Operating Periods (IOPs) were conducted
122 during 2014, with IOP2 taking place during the dry season from the 15th of August through the 15th of
123 October 2014 [35]. This campaign was conducted over central Amazonia with multiple sampling sites
124 around the city of Manaus (Figure 1). Northeasterly trade winds in this region dictate the general wind
125 direction over the area and so the sampling sites were located with this in mind. These trade winds carry
126 marine aerosols from the ocean inland and, during the wet season, can also carry supermicron mineral
127 dust from the Sahara [37]. For the wet season, secondary organic aerosols (pure liquid or with a
128 soot/inorganic core) dominate the submicrometer size range [38-40]. During the dry season, however, a
129 large fraction of the aerosol population can be attributed to large scale biomass burning [31].

130 For this study, particle samples from three sampling sites were studied: The Amazon Tall Tower
131 Observatory (ATTO; T0a), the Terrestrial Ecosystem Science site (ZF2; T0t), and the Atmospheric
132 Radiation Measurement (ARM) site located near Manacapuru (T3). The ATTO site is located
133 approximately 150 km upwind of Manaus and serves as a background site. During the wet season near-
134 pristine conditions can be observed here but, because the dry season is dominated by biomass burning
135 particles, the ATTO site will serve as a regional background rather than a background of pure biogenic
136 particles as might be expected [41]. The ZF2 site is located about 140 km directly downwind of the ATTO
137 site. The final site, T3, is 70 km downwind of Manaus and often experiences the pollution plume from

138 Manaus [35,36]. Site locations and characteristics are presented in Martin et al. 2016 [35]. For additional
 139 background information about the sampling sites please see Andreae et al., 2015, Artaxo et al., 2013, and Martin
 140 et al., 2016 [29,35,41].



141 **Figure 1.** Positions of the three sampling sites located around the city of Manaus with representative
 142 National Oceanic and Atmospheric Administration (NOAA) Hybrid Single Particle Lagrangian Integrated
 143 Trajectory Model (HYSPLIT) back trajectories (14/Sept from 9:00 to 12:00 shown, 500 m starting elevation
 144 using the global data assimilation system data set) [42,43]. (Inset) Overview map of South America with
 145 the region of interest circled. Longer back trajectories as well as varied starting elevations for the three
 146 sites are shown in Figure S1. [29,35,41]

147 2.2. Sample Collection:

148 At the three sampling sites, atmospheric particle samples were collected on silicon nitride (Si_3N_4)
 149 membranes overlaid on a 5 x 5 mm silicon chip frame with a central 0.5 x 0.5 mm window (100 nm thick
 150 membrane, Silson Inc.). Samples were collected using a Micro-Orifice Uniform Deposit Impactor
 151 (MOUDI, MSP MOUDI-110) on the dates and times shown in Table 1. HYSPLIT back trajectories were
 152 examined for each sampling period to confirm the wind patterns seen in Figure 1. These samples were
 153 then analyzed sequentially with the two spectromicroscopy techniques discussed in the following
 154 sections.

155 **Table 1.** Samples examined for this study. The nominal size range for MOUDI stage 7 is 0.56 – 0.32 μm
 156 and stage 8 is 0.32 – 0.18 μm .

Site	Date (2014)	Time Period (Local Time)	MOUDI Stage	# of Analyzed Particles
ATTO	14-15/Oct	19:00 (14/Oct) – 19:00 (15/Oct)	7	501
	12-13/Sept	Night 18:00-6:00	7	334
T3	13/Sept	Day 8:00-12:00	7	279
	13/Sept	Day 8:00-12:00	8	59 ¹

	14/Sept	Day 9:00-12:00	7	182
	14/Sept	Day 9:00-12:00	8	50 ¹
	3-6/Oct	11:00 (3/Oct) – 11:00 (6/Oct)	7	315
ZF2	6-8/Oct	14:00 (6/Oct) – 12:00 (8/Oct)	7	309
	6-8/Oct	14:00 (6/Oct) – 12:00 (8/Oct)	8	967

¹Low particle counts are due to low particle loading of microscopy samples and time constraints

157

158 2.3. STXM Data Collection and Image Processing:

159 Samples were first imaged at the STXM beamline 5.3.2.2 at the Advanced Light Source (ALS) [44].
 160 The energy range of this STXM (200-600 eV) end station enables the quantitative study of carbon,
 161 nitrogen, and oxygen. Energy selected soft X-rays were focused down to a ~30 nm spot size and directed
 162 onto the sample surface. After a suitable 15x15 μm region was located, the sample stage was then raster
 163 scanned, with 40 nm steps, using piezo-electric stages to capture an image at a specific energy. This
 164 process was then repeated at multiple photon energies to produce a stack of images with an absorption
 165 spectrum associated with each 40x40 nm pixel. For each element, photon energies were chosen before
 166 and after the k-shell absorption edge: 278 and 320 eV for carbon, 400 and 430 eV for nitrogen, and 525
 167 and 550 eV for oxygen [45]. Additional images were also taken near the carbon edge at 285.4 and 288.5
 168 eV, for the RC=CR and RCOOR C1s→π* transitions respectively, in order to partly characterize the
 169 molecular speciation of carbon [46].

170 Any displacement between images within a stack is corrected by a routine based on Guizar-Sicarios'
 171 image registration algorithm [47]. Regions within a given stack were then identified as particles or
 172 substrate using Otsu's method on that stack's average intensity image over all 8 energies [48].
 173 Background subtraction of a given element's pre-edge intensity image from its post-edge image is then
 174 performed to account for any absorbing species not attributed to that element.

175 The recorded intensity at each pixel determined to be a particle was converted to optical density
 176 using:

$$OD = -\ln\left(\frac{I}{I_0}\right) \quad (1)$$

177 where OD is optical density, I is intensity of the pixel, and I₀ is the background intensity. This is followed
 178 by a conversion to mass with the following formula:

$$m = \frac{OD * A}{\mu_{post} - \mu_{pre}} \quad (2)$$

179 where *m* is the mass of a specific element at that pixel, *A* is the area of that pixel, and μ_{pre} and μ_{post} refer to
 180 the mass absorption coefficients for that specific element before and after the absorption edge,
 181 respectively. Mass absorption coefficients have been both empirically and theoretically determined for a
 182 variety of elements as tabulated in Henke et al., 1993 [45].

183 Previously developed algorithms for determining the speciation of carbon using 278, 285.4, 288.5,
 184 and 320 eV were applied to each Field Of View (FOV) as well. This mapping technique uses a series of
 185 thresholds to identify inorganics, soot, and organic carbon. Total carbon is taken to be OD₃₂₀ – OD₂₇₈,
 186 pixels with an OD₂₇₈/OD₃₂₀ ratio 0.5 or greater are rich in inorganics, and pixels with an elevated (0.35)
 187 ratio of sp² bonding compared to total carbon (OD_{288.5} – OD₂₇₈)/(OD₃₂₀ – OD₂₇₈) are indicative of soot [46].

188 2.4. SEM/EDX Data Collection:

189 The same sample windows previously imaged with STXM were imaged again with a computer
 190 controlled scanning electron microscope (FEL, Quanta 3D FEG) coupled with energy dispersive X-ray

191 spectroscopy (CCSEM/EDX). The SEM utilized a field emission tip to produce an electron beam which
 192 was directed and focused onto a sample with an accelerating voltage of 20 kV which can cause core shell
 193 atomic electrons to be ejected from the sample. Higher shell electrons then relax into the newly created
 194 orbital hole, releasing an elementally characteristic photon recorded by an energy dispersive X-ray
 195 detector (EDAX PV7761/54 ME with Si(Li) detector). As the electron beam was scanned over the sample,
 196 the transmitted electron image was used to identify the exact same FOVs from the previous STXM
 197 images. Once a FOV previously analyzed with STXM is located, a 10,000x image (30 nm/pixel resolution)
 198 was captured. This image combines both transmitted and backscattered electron images to improve
 199 particle detection [24]. A threshold contrast level was then set to identify which areas of the collected
 200 image counted as particles using the “Genesis” software from EDAX, Inc. A software filter was then
 201 applied which discounts particles that are too small (e.g. noise spikes) or too large (e.g. multiple nearby
 202 particles counted as a single large particle). The electron beam was then directed towards each identified
 203 particle in sequence and an EDX spectrum was collected. Afterwards software was used to fit the peaks
 204 of eleven relevant elements selected for this study: Na, Mg, P, S, Cl, K, Ca, Mn, Fe, Ni, and Zn. Some
 205 elements of interest have been included in the spectral fit, but omitted from quantitation, including Al, Si,
 206 and Cu due to background sources of these elements: 1) the STXM sample holder where the Si₃N₄
 207 windows sat was made of Al and was inserted into the SEM as well, 2) the mounting stage that holds
 208 samples inside the microscope was fabricated from beryllium-copper alloy, 3) the EDX data was collected
 209 using a Si(Li) detector with a 10 mm² active area. Each of these circumstances could contribute
 210 background signal for the elements in question.

211 After data has been collected from both SEM and STXM, individual particle mass information is
 212 contained in two sets of images: one from STXM and one from SEM. Due to differing contrast
 213 mechanisms, image resolution, and other factors, particles do not necessarily appear the same between
 214 images taken with the two techniques. The manual matching of particles was performed using pattern
 215 recognition to ensure proper alignment of the image sets from both techniques.

216 2.5. Quantifying Higher Z Elements:

217 Using the aforementioned methods, STXM yields quantitative, absolute mass information on a sub-
 218 particle basis. SEM/EDX is more limited in this aspect, being quantitative for elements with Z>11 (Na)
 219 but only semi-quantitative for C, N, and O [24]. Due to the EDAX software used for EDX data collection
 220 and analysis, there is an additional caveat to the quantitation of Z>11 elements: the software reports only
 221 the relative mass percentages compared to the elements chosen during data processing. In order to
 222 properly quantify the mixing state, the absolute mass of each element in each particle is necessary. To
 223 determine these absolute masses, a system of equations was set up using the following equation types:

$$224 \quad OD_i = \rho t \sum_{a=1}^A f_a \mu_{a,i} \quad (3)$$

$$225 \quad \frac{f_x}{f_y} = \frac{rel.\%_x}{rel.\%_y} \quad (4)$$

$$226 \quad \sum_{a=1}^A f_a = 1 \quad (5)$$

227 For each pixel, OD_i is the optical density taken at energy i , ρ is the density and t is the thickness of the
 sample (at that pixel), f_a is the mass fraction of element a , and $\mu_{a,i}$ is the mass absorption coefficient of
 element a at energy i . Equation 4 is a general relationship, which equates the ratio of two absolute mass
 fractions (f_x and f_y) with the ratio of relative mass percentages ($rel.\%_x$ and $rel.\%_y$) produced by the EDAX

228 software. Equation 3 utilizes the quantitative nature of STXM whereas the relative mass percent of
 229 elements with $Z > 11$ were used in equation 4 to combine the quantitative abilities of SEM/EDX. This
 230 system was then solved for the 14 absolute mass fractions (f_a) of each element chosen in this study.

231 Equation 5 is an assumption that is valid when the 14 elements analyzed comprise close to 100% of
 232 the particle's composition. Here, systematic error in the calculated mass fractions of specific particles can
 233 be introduced in particles where elements not considered represent a significant portion of that particle's
 234 mass (e.g. mineral dust and Si or Al). During the Amazonian dry season, Al and Si represent 0.3% and
 235 0.4% of the average fine mode particle mass [49]. This mass fraction error becomes negligible, however,
 236 when the ensemble diversity values or mixing state index is considered due to the overwhelming mass of
 237 C, N, and O in each particle.

238 After both sets of images are matched and the corresponding light and heavy element information
 239 has been processed quantitatively, mass information for each FOV is contained in sets of maps, one for
 240 each element analyzed.

241 2.6. Mixing State Parameterization:

242 The method of parameterizing mixing state used here is based on calculating mass fractions for
 243 different groupings of the individual components defined and is reproduced from Riemer and West [21].
 244 The absolute mass of a given component a , within a given particle i , is labeled as m_i^a where $a = 1, \dots, A$
 245 (and A is the total number of components) and $i = 1, \dots, N$ (the total number of particles). From this, the
 246 following relationships are established:

$$\sum_{a=1}^A m_i^a = m_i \text{ (Mass of } i^{\text{th}} \text{ particle)} \quad (6)$$

$$\sum_{i=1}^N m_i^a = m^a \text{ (Mass of } a^{\text{th}} \text{ component)} \quad (7)$$

$$\sum_{a=1}^A \sum_{i=1}^N m_i^a = m \text{ (Total mass of sample)} \quad (8)$$

247 Mass fractions are then established from these relationships with:

$$f_i = \frac{m_i}{m}, \quad f^a = \frac{m^a}{m}, \quad f_i^a = \frac{m_i^a}{m_i} \quad (9)$$

248 Where f_i is the mass fraction of a particle within a sample, f^a is the mass fraction of component a within a
 249 sample, and f_i^a is the mass fraction of component a within particle i .

250 These mass fractions are used to calculate the Shannon entropy (also called information entropy) for
 251 each particle, each component, and for the bulk using Equations 10, 11, and 12 respectively.

$$H_i = \sum_{a=1}^A -f_i^a \ln f_i^a \quad (10)$$

$$H_\alpha = \sum_{i=1}^N f_i H_i \quad (11)$$

$$H_{\gamma} = \sum_{a=1}^A -f^a \ln f^a \quad (12)$$

252 Each type of mass fraction can be thought of as a probability, and thus the collection of mass
 253 fractions defines a probability distribution. The Shannon entropy of a probability distribution quantifies
 254 how uniform the distribution is. Shannon entropy is maximized if every element in the distribution is
 255 equally probable, and the entropy decreases the more likely any individual element becomes [21]. With
 256 this information entropy, diversity values are defined with the following equations

$$D_i = e^{H_i}, \quad D_{\alpha} = e^{H_{\alpha}}, \quad D_{\gamma} = e^{H_{\gamma}} \quad (13)$$

257 The diversity values contain the same type of information, but represent it in another way. Each
 258 diversity value represents the effective number of species (weighted by mass) within a given population
 259 (i.e. D_i represents the number of species within a specific particle, D_{α} is the average number of species
 260 within any given particle, and D_{γ} represents the number of species within the entire sample). From these
 261 diversity values the mixing state index is defined as

$$\chi = \frac{D_{\alpha} - 1}{D_{\gamma} - 1} \quad (14)$$

262 This definition compares how many species exist, on average, within individual particles, with the
 263 total number of species identified in the sample. χ is at a minimum of 0 when D_{α} is 1, corresponding to
 264 each particle being comprised of exactly one species. A mixing state index of 1 occurs when D_{α} and D_{γ}
 265 are equal, meaning that each particle has the same composition as the bulk sample.

266 2.7. Error in Mixing State Index, χ

267 The measurement uncertainty of χ due to STXM, EDX, or the system of equations was found to be
 268 insignificant compared to the statistical uncertainty of χ within each cluster and thus only the statistical
 269 uncertainty is considered here. To determine this uncertainty, the statistical uncertainty in D_{α} , and D_{γ}
 270 were found separately.

271 Determining statistical uncertainty in D_{γ} starts with f^a from Equation 9. From Riemer and West [21],
 272 f^a is a ratio of the total mass of the a^{th} component and the total mass of the sample, however this is
 273 equivalent to the ratio of the mean mass of the a^{th} component and the mean mass of particles within the
 274 sample:

$$f^a = \frac{m^a}{m} = \frac{\sum_{i=1}^N m_i^a}{\sum_{i=1}^N \sum_{a=1}^A m_i^a} = \frac{\frac{1}{N} \sum_{i=1}^N m_i^a}{\frac{1}{N} \sum_{i=1}^N \sum_{a=1}^A m_i^a} = \frac{\overline{m^a}}{\overline{m}} \quad (15)$$

275 where $\overline{m^a}$ is the mean mass of the a^{th} component and \overline{m} is the mean mass of particles within the sample.
 276 From this, the standard error (for a 95% confidence level) can be determined for $\overline{m^a}$ and \overline{m} which is then
 277 propagated through Equations 9-13.

278 The statistical uncertainty in D_{α} was found by first rearranging and combining Equations 11 and 13:

$$H_{\alpha} = \sum_{i=1}^N f_i \ln D_i \quad (16)$$

279 and, because this takes the form of an expected value $E(x) = \sum f_x x$, the error in H_{α} can be found with
 280 Equation 15 and then propagated with Equation 16 to determine the error in D_{α} .

281 2.8. k-Means Clustering:

282 All analyzed particles were combined and a k-means clustering algorithm was then used to group
283 particles into clusters [50]. A vector of 18 variables were used for k-means clustering: the quantitative
284 elemental mass fractions composition of the 14 elements chosen, the Circular Equivalent Diameter (CED)
285 [1], D_i , the mass fraction of carbon attributed to soot, and the area fraction of the particle dominated by
286 inorganics. In this way, particles were clustered based on size, elemental composition, as well as on how
287 carbon speciation was distributed. The square root of these parameters was used in the clustering
288 algorithm to enhance trace elements in accordance with Rebotier et al. [51]. CED is used here as the
289 descriptor of particle size due to it being readily calculable from STXM data. While aerodynamic
290 equivalent diameter is the physical parameter determining MOUDI sampling, it is difficult to retrieve
291 from microscopy data.

292 The correct number of clusters was initially chosen based on a combination of two common
293 methods: the elbow method, and the silhouette method [52]. Using these two methods, 12 clusters were
294 identified.

295 3. Results:

296 As a general trend, during the dry season, the whole Amazon Basin experiences a significantly
297 higher aerosol number concentration and $\text{CO}_{(g)}$ concentration compared to the wet season, largely due to
298 in-Basin fires [31,41]. Furthermore, in addition to biomass burning, emissions from Manaus are often
299 observed at the T3 site (downwind of Manaus), sporadically at the ZF2 site (upwind but near the city)
300 and rarely at ATTO (upwind and ~150 km away). Table 2 outlines some supporting measurements made
301 at the three sites.

302 Most values listed for the 12/Sept and 13/Sept sample at T3 are consistent with their sample-period
303 monthly averages, even considering time of day each sample was collected. The data from 14/Sept,
304 however, shows a marked increase in particle concentration, nitrate, organic, and CO concentration,
305 along with a small increase in BC. This is indicative of a heavy pollution plume which, in this case, had
306 recently passed over the T3 sampling site (see Figure S2). AMS and particle concentration data for the T3
307 sites show a reasonable agreement with either background or polluted conditions previously reported, as
308 do ozone measurements [53,54]. The monthly average values for 13/Sept and 14/Sept are often similar
309 due to the similar (though not identical) sampling time from 8:00 to 12:00 and from 9:00 to 12:00
310 respectively. The similarity between monthly average particle concentrations for 12/Sept and 13/Sept are
311 purely coincidental.

312 Particle concentration and AMS/ACSM data were not available for the ZF2 site during this study.
313 Concentrations of CO, ozone, and BC values agreed well with their sample-period monthly averages with
314 the lone exception of ozone levels for the 3-6/Oct sample period. This increase is also reflected, albeit to a
315 much lesser degree, in an increase of CO and BC levels. From Figure S3 it appears that sample collection
316 began in the middle of a period of higher than average pollution levels. Temporary enhancements in BC
317 due to emissions from Manaus have been observed previously at ZF2 [55]. Overall the levels of CO,
318 ozone, and BC at ZF2 are smaller with respect to T3 values as is expected. ACSM data collected for past
319 studies at site ZF2 fits well with the trends seen in the limited data presented here [29]. Concentrations of
320 aerosol components can fluctuate depending on the day but September (2012) averages for ammonium,
321 chloride, nitrate, organics, and sulfate have been reported as 0.46, 0.01, 0.22, 13.9, 0.37 $\mu\text{g m}^{-3}$ respectively
322 by Artaxo et al., 2013.

323 Unsurprisingly, the ATTO site shows the lowest levels of almost all presented aerosol and gas
324 components. The sample collected on 15/Oct also appears to be fairly average with respect to the sample-
325 period monthly average for this collection time. The low particle concentration suggests a sample with
326 low pollution levels which makes this sample ideal for our purposes. The values presented for the
327 ATTO site are also in fair agreement with previously published data [41].

328 The supporting data tabulated here has been collected from different instruments at the three sites
 329 and so a direct comparison could be suspect, especially in the case of BC measurements [56]. However,
 330 considering the agreement with published literature and qualitative use of Table 2 in the current work,
 331 we believe any associated error is acceptable.

332 **Table 2.** Supporting data during sampling times for each sampling site. Values listed under sample dates
 333 are averages over that sampling period. Values in the adjacent (Avg.) column are monthly averages only
 334 for the hours coinciding with the sampling times listed in Table 1 (e.g. the average particle concentration
 335 between the hours of 8:00 and 12:00 averaged over the entire month for the Avg. column next to 13/Sept).
 336 Ammonium, chloride, organics, sulfate, and Black Carbon (BC) pertain to aerosol measurements whereas
 337 CO_(g) and O_{3(g)} are gas phase measurements. Measurements with blank values were not available during
 338 the period of this study. Information regarding collection conditions can be found in Andreae et al., 2015,
 339 Artaxo et al., 2013, Martin et al., 2016 [29,35,41].

	T3				ZF2				ATTO			
	12/S ept (night)	Av g.	13/S ept (day)	Av g.	14/S ept (day)	Av g.	3- 6/Oc t	A vg.	6- 8/Oct	A vg.	15/ Oct	Av g.
Particle Conc. (cm ⁻³)	2400 ¹⁰	340 ⁰¹⁰	2400 ¹⁰	340 ⁰¹⁰	5800 ¹⁰	340 ⁰¹⁰	-	-	-	-	110 ⁰¹¹	140 ⁰¹¹
Ammonium (µg m ⁻³)	0.33 ¹	0.4 ⁵	0.34 ¹	0.4 ²	0.28 ¹	0.4 ²	-	-	-	-	0.23 ²	0.2 ⁰
Chloride (ng m ⁻³)	14.9 ¹	20 ¹	17.0 ¹	27 ¹	24 ¹	27 ¹	-	-	-	-	14.4 ²	14. ⁹
Nitrate (µg m ⁻³)	0.11 ¹	0.1 ⁶	0.20 ¹	0.1 ⁹	0.28 ¹	0.1 ⁹	-	-	-	-	0.16 ²	0.1 ⁵
Organics (µg m ⁻³)	7.9 ¹	10. ⁷	7.6 ¹	10. ⁰	14.1 ¹	10. ⁰	-	-	-	-	3.8 ²	4.4 ²
Sulfate (µg m ⁻³)	1.0 ¹	1.4 ¹	0.86 ¹	1.1 ¹	0.71 ¹	1.1 ¹	-	-	-	-	0.53 ²	0.6 ¹
CO _(g) (ppb)	178 ³	210 ³	211 ³	257 ³	558 ³	254 ³	178 ⁴	16 ⁹	159 ⁴	16 ⁸	141 ⁴	138 ⁴
O _{3(g)} (ppb)	8 ⁵	9 ⁵	36 ⁵	29 ⁵	43 ⁵	32 ⁵	17 ⁶	13 ⁶	12 ⁶	13 ⁶	-	-
BC (µg m ⁻³)	0.8 ⁷	0.9 ⁷	1.0 ⁷	1.0 ⁷	1.2 ⁷	1.0 ⁷	0.5 ⁸	0.4 ⁸	0.6 ⁸	0.4 ⁸	0.5 ⁹	0.4 ⁹

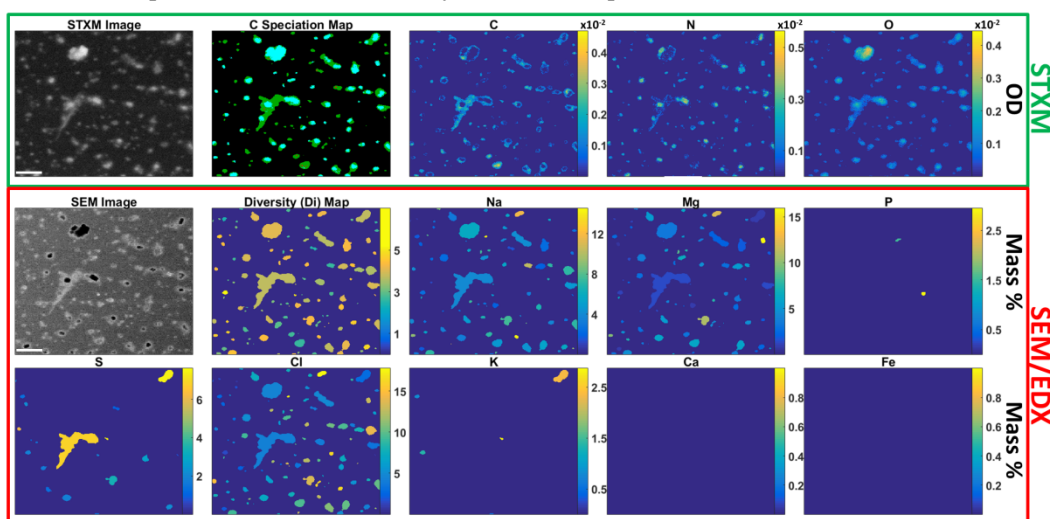
340 ¹Aerosol Mass Spectrometer (AMS), ²Aerosol Chemical Speciation Monitor (ACSM), ³ARM/Mobile Aerosol
 341 Observatory System (MAOS) Los Gatos ICOS™ Analyzer, ⁴Picarro Cavity Ringdown Spectrometer (CRDS),
 342 ⁵ARM/MAOS Ozone Analyzer, ⁶Thermo 49i, ⁷ARM/AOS Aethalometer, ⁸MultiAngle Absorption
 343 Photometer (MAAP)-5012, ⁹MAAP-5012, ¹⁰ARM/MAOS Scanning Mobility Particle Sizer (SMPS), ¹¹SMPS

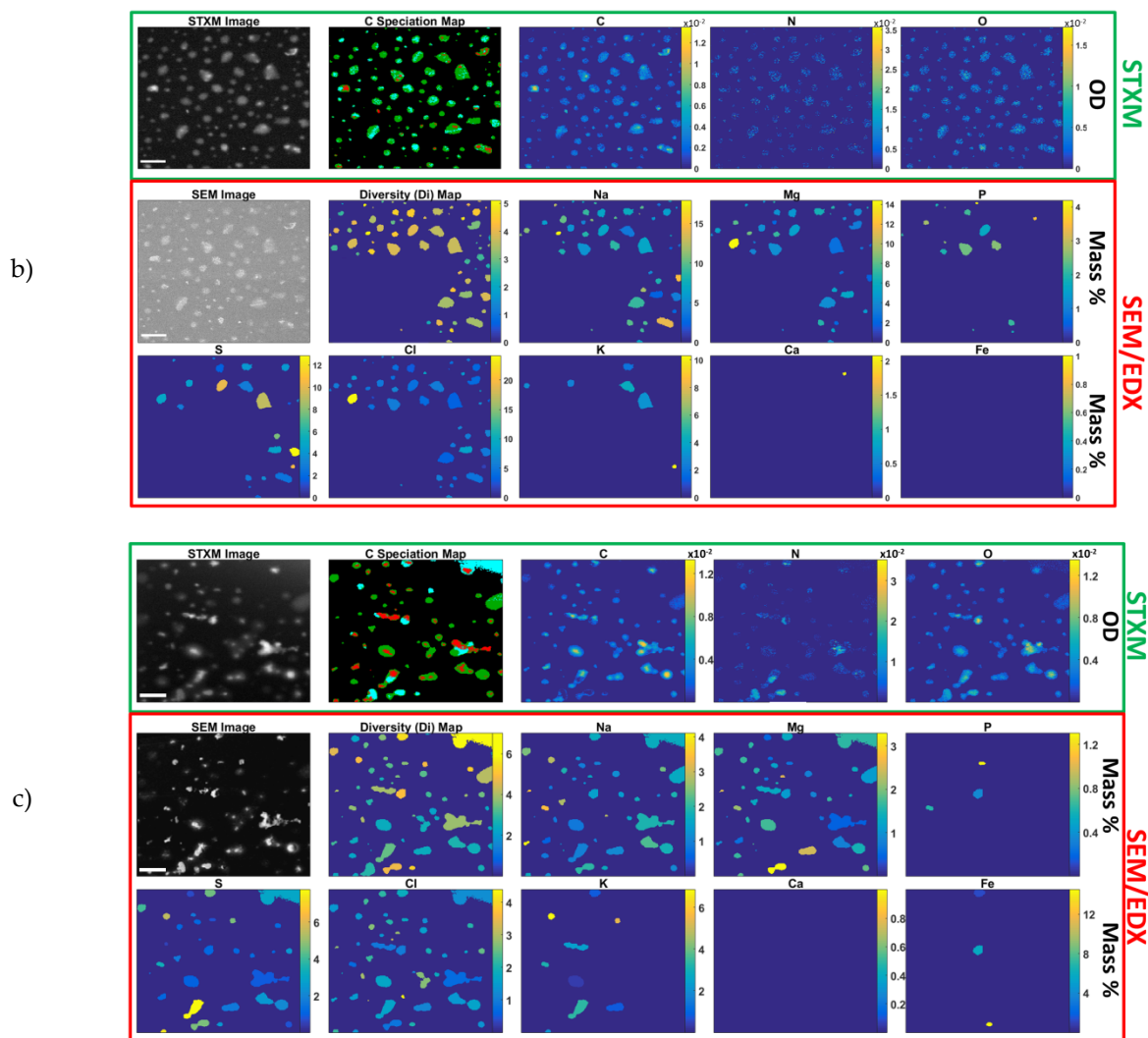
344 Figure 2 shows an example FOV and the type of data calculated for all three sites. Each particle has
 345 an OD map (which is proportional to mass, refer to Equation 2) for C, N, and O as well as a C speciation
 346 map. In Figure 2 the STXM grayscale image shown is the average intensity map over the four C edge
 347 images. There is a correlation between the brightest spots and the identification of soot in the C
 348 speciation map. This speciated image is possible due to the sub-particle spatial resolution achievable
 349 with STXM mapping, which is highlighted in the C, N, and O maps. Potential inter-site differences can
 350 be seen in this figure: the ATTO sample shows large inorganic inclusions coated by organics along with
 351 Na, Mg, and Cl representing the bulk of the higher Z elements. The particles present at ATTO also often

352 look like either inorganic aerosols from biomass burning events or small biogenic K salt particles (due to
353 the KCl or NaCl inorganic cores), or secondary organics, with a few particles appearing to be sea spray
354 [57-59]. The ZF2 sample has a consistent circular morphology with appreciable mixing between the three
355 carbon species. ZF2 particles often look amorphous with some particles appearing to be sulfate-based
356 aerosols [60]. Lastly, the T3 sample is the most varied in terms of morphology and in elemental
357 composition with S, P, and K all present in many of the particles sampled. Unsurprisingly, soot
358 inclusions are much more common in the T3 sample. Particles from this site often look like biomass
359 burning particles with a few fractal soot particles as well [61]. It is important to keep in mind that the
360 particle morphologies presented have possibly changed from their original state when collected. This
361 change could be due to the impaction of particles during sampling, or the changes in relative humidity
362 experienced as these particles are collected, stored, transported, and placed in vacuum before STXM or
363 SEM images can be obtained. Liquid particles can spread upon impact making them appear larger on
364 microscopy substrates. Particles with high water content can effloresce at lower relative humidity leaving
365 solid phase inorganic components. Loss of highly volatile organic carbon or volatile inorganics like
366 ammonium nitrate is also possible, making concentrations detected here a lower limit for inorganic and
367 organic species.

368 The SEM grayscale image shows the slightly different views presented by the two techniques, with
369 particle shapes appearing different between them along with a higher spatial resolution image (10 nm vs.
370 40 nm with STXM). Soot inclusions identified in the C speciation map are also seen as bright spots in the
371 SEM grayscale image in addition to many of the inorganic inclusions [24]. From the EDX data collection,
372 mass fraction maps for each element (on a per-particle basis) were used to calculate individual particle
373 diversity (D_i) values for each particle. Another aspect of the maps is the varying background level
374 between SEM images, seen especially in the high background of the ZF2 image. This is a consequence of
375 the brightness and contrast levels being set before EDX acquisition and was performed to ensure that the
376 maximum number of particles were detected by the CCSEM particle detection software.

a)





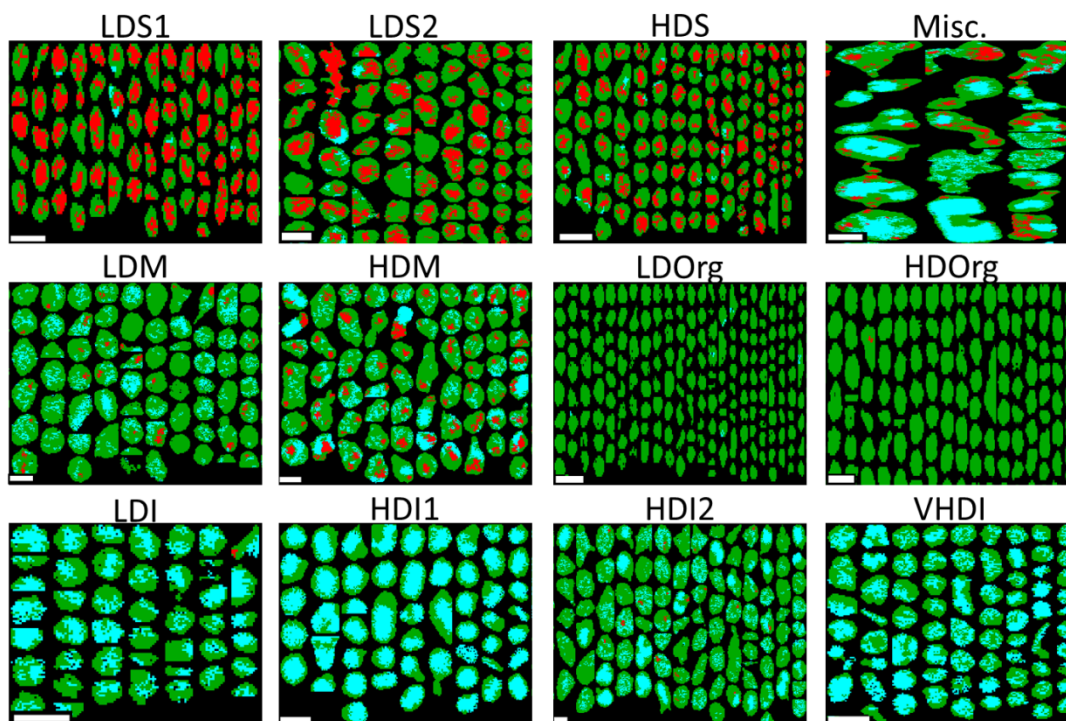
377 **Figure 2.** Raw and processed image maps for selected FOVs from a) the ATTO site collected on
 378 15/Oct/2014, b) the ZF2 site collected on 3-6/Oct/2014, and c) the T3 site collected on 13/Sept/2014. Raw
 379 images for STXM and SEM are shown (with 2 μm scale bar in bottom left) along with false color maps
 380 showing the sub-particle (for C, N, and O) or per-particle (for higher Z elements) mass distribution. Also
 381 shown is a color coded carbon speciation map showing soot (red), inorganic (teal), and organic (green)
 382 carbon. The calculated individual particle diversity (D_i) is also shown. Note the large spot in the upper
 383 right corner of the T3 sample, this was most likely the edge of the Si_3N_4 window and was removed from
 384 calculations. Also note the empty lower left corner in the ZF2 sample EDX data lacking for those particles;
 385 because of this they were removed. Zn, Mn, and Ni maps are omitted here as they were not detected in
 386 these FOVs.

387 3.1. Clustering and Source Attribution:

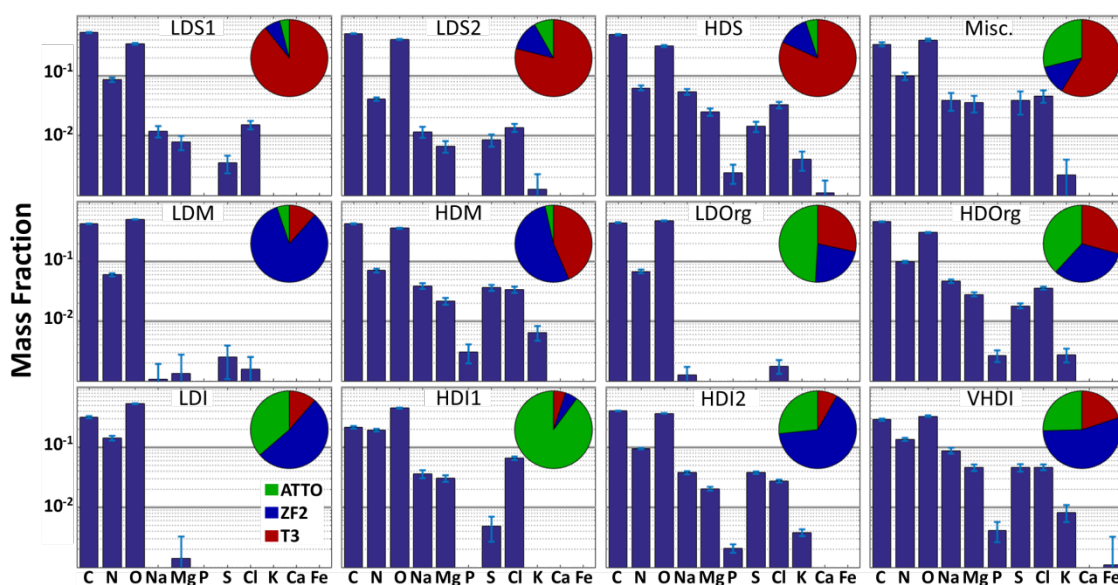
388 For each of the 12 clusters, determined by the k-means algorithm, a random representative sample of
 389 40 particles (taken from any sample or sampling site) was selected for the images shown in Figure 3. The
 390 average elemental composition of each cluster is shown in Figure 4 along with the fraction of each cluster
 391 collected at the three sampling sites. Finally, Table 3 outlines the assigned colors and labels, as well as
 392 some relevant descriptive statistics for each cluster. As can be seen in the average particle diversity

393 column in Table 3, most clusters have a D_{α} value near either 2.4 or 3.6 (with a single exception). These
394 two values define the “low” or “high” diversity referred to in the cluster names and are discussed in
395 more detail in section 3.5. A similar source apportionment was discussed in a previous SEM based study,
396 however, it was conducted during the wet season when biogenic aerosols dominate [38]. During the dry
397 season, these biogenic particles are still present but are overwhelmed by aerosols derived from biomass
398 burning.

399 One notable aspect of Figure 4 is the ratio of elemental Cl to S in each of the clusters shown. From
400 the EDX spectroscopy data presented here, the mass fraction of Cl is often greater or at least similar to
401 that of S. This is apparently contradicted by Table 2, where the concentrations of chloride are an order of
402 magnitude less than the concentrations of sulfate. There are, however, a few extenuating circumstances
403 for this comparison. Firstly, the chloride level in Table 2 is that of non-refractory material owing to the
404 AMS’s method of volatilizing particles at ~ 600 °C. This is well below the vaporization temperature for
405 NaCl and KCl, two major sources of Cl (and inorganics in general). Hence, Table 2 AMS data
406 underestimates Cl mass fractions. Another requirement to allow direct comparison is to change
407 concentration of sulfate to S by multiplying by the ratio of molar masses ($\sim 32/96$), reducing the
408 concentrations seen in Table 2 to about one third. The third circumstance is the potential for beam
409 damage using the two sequential microscopy techniques here. Some of the inorganic inclusions/cores
410 detected using STXM/NEXAFS spectroscopy may be particularly sensitive to electron beam damage.
411 These sensitive inorganics (particularly ammonium sulfate) could have been volatilized during the
412 scanning/locating phase of SEM and therefore would not be well characterized with subsequent EDX
413 spectroscopy. This carries two consequences: a possible underestimation in the mass fraction of S, and
414 the identification of inorganic regions with STXM without the detection of many inorganic elements by
415 EDX to explain the inclusions. This issue of S quantification is further highlighted when the S/Cl ratios in
416 Figure 4 are compared with previous Particle Induced X-ray Emission (PIXE) measurements which report
417 aerosol S concentrations an order of magnitude greater than Cl concentrations [62,63]. In addition to
418 PIXE, Artaxo et al., 1994 used factor analysis to determine broad particle classes including soil dust,
419 biogenic, marine, and biomass burning classes. One finding of relevance is the high degree of correlation
420 between biogenic particles and S concentration [63]. For the current work, this could suggest an
421 underestimation in the number of clusters hypothesized to contain biogenic particles.



422 **Figure 3.** Random sample of ~40 particles from each cluster showing sub-particle carbon speciation as
 423 either soot (red), inorganic (teal), or organic (green). 1 μm scale bars are shown in the bottom left of each
 424 image. Cluster identification (image labels) is provided in Table 3.



425 **Figure 4.** Average elemental composition of each cluster with inset pie chart showing each cluster's
 426 representation at the three sampling sites: ATTO (green), ZF2 (blue), and T3 (red). Al and Si were not
 427 included due to the background from the Al sample holder and the Si₃N₄ substrate. Mn, Ni, and Zn were
 428 not detected and so are omitted here. Cluster identifications (image labels) are provided in Table 3.

429

Table 3. Cluster identifying information

Cluster Name	Label	Avg. Diversity, D α (Std Err)	CED, μm (Std Err)	O/C Ratio ²	N
Sub- μm Low Diversity Soot	LDS1	2.67 (0.24)	0.37 (0.01)	0.49	26 1
Super- μm Low Diversity Soot ¹	LDS2	2.74 (0.29)	1.04 (0.06)	0.60	18 0
High Diversity Soot	HDS	3.49 (0.51)	0.52 (0.02)	0.48	18 3
Low Diversity Organics	LDOrg	2.36 (0.08)	0.29 (0.01)	0.81	54 0
High Diversity Organics	HDOrg	3.49 (0.36)	0.34 (0.01)	0.50	64 7
Low Diversity Inorganics	LDI	2.57 (0.17)	0.39 (0.02)	1.26	16 0
High Diversity Coated Inorganics	HDI1	3.87 (0.60)	0.62 (0.03)	1.57	20 1
High Diversity Inorganics	HDI2	3.75 (0.26)	0.75 (0.02)	0.69	65 5
Very High Diversity Inorganics	VHDI	4.83 (1.92)	0.45 (0.03)	0.86	21 2
Low Diversity Mixed	LDM	2.43 (0.13)	0.91 (0.04)	0.88	22 1
High Diversity Mixed	HDM	3.73 (0.72)	0.94 (0.04)	0.63	20 9
Miscellaneous	Misc.	3.83 (2.10)	2.35 (0.22)	0.89	47

430

431

432

433

¹While MOUDI stages 7 and 8 are nominally submicron stages, it is possible for larger particles to bounce from upper stages and be found in smaller stages. The sub/supermicron descriptor here is also based on circular equivalent diameter rather than aerodynamic diameter like the MOUDI stage cut-off values. ²O/C ratio calculated for entire particles including organics and inorganics.

434

3.1.1. Soot Clusters (LDS1, LDS2, HDS)

435

436

437

438

439

440

441

442

443

The HDS cluster is characterized by a thick organic coating around a soot core. The high levels of organics and K suggests that this cluster mostly originated from biomass burning, but may also contain urban emissions [64]. This, combined with the overwhelming majority of HDS particles being from site T3, suggests that they are predominantly anthropogenic in nature. This cluster's enhanced mass fraction of Na, Cl, Mg, and S indicates a contribution from marine aerosols. Together with the appreciable amount of P and K this results in the higher particle diversity seen in this cluster. Further supporting this cluster's identity is that enhancement of these elements have been observed previously during biomass burning events in the presence of a background rich in marine aerosols [65,66].

444

445

446

447

In addition to LDS1 lacking the P, K, and Ca that HDS has, LDS1 also has a smaller amount of Na, Mg, S, and Cl which results in the lower average particle diversity. The decreased abundance of K and Cl may indicate urban combustion sources such as diesel engines as opposed to biomass burning [57]. The coatings of organics around the soot cores seen in this cluster are much thinner compared to other soot containing clusters which suggests that particles in this cluster are less aged [67]. The vast majority of

448 particles from this cluster type are from site T3; given that T3 is downwind of Manaus, this suggests fresh
449 urban soot emissions as this cluster's source [36].

450 The large and multiple soot inclusions and the presence of fractal soot are indications that LDS2 is
451 comprised of particles with a contribution from combustion [68,69]. Particles in LDS2 are found mostly at
452 site T3 which points towards Manaus being the source of these aerosols. The sometimes substantial
453 organic coating on many of these particles is most likely due to condensation during travel of fresh
454 aerosols from Manaus travel to the T3 sampling site. With the exception of the one night time sample, all
455 T3 samples were collected during the mid to late morning (~9:00 to 12:00) which has been seen in other
456 urban areas to correspond to an increased in aged soot over fresh soot owing to the increase in
457 photochemistry [5].

458 3.1.2. Organic Clusters (LDOrg, HDOrg)

459 HDOrg is comprised of small particles with their carbon being entirely organic dominant. This
460 cluster has a substantial amount of the heavier elements ($Z=11$ (Na) and above) driving the diversity up.
461 The presence of P specifically is important as these elements, coupled with the carbon speciation, suggest
462 that the particles from this cluster are biological in origin [62]. This cluster also contains the highest
463 number of particles with collocated Na and S, which has been previously shown to suggest biogenic
464 particles [70]. The HDOrg cluster also contains an appreciable amount of K and, given that one sample
465 was taken at night, could include biological particles derived from fungal spores [59].

466 LDOrg is similar in carbon speciation, morphology, and size but lacks the heavier elements
467 contained in HDOrg. The almost entirely C, N, and O composition, small size, and the organic carbon
468 speciation suggest that particles in this cluster are secondary organic aerosols. This is supported by a
469 slight majority of particles in this cluster coming from the general direction of the ATTO site, where a
470 dominant appearance of biogenic secondary organic aerosols and a smaller influence from anthropogenic
471 emissions is expected. The high O/C ratio, along with the dearth of inorganics, may make this cluster
472 comparable to aged ambient oxygenated aerosols [71].

473 As discussed further on in section 3.2, both organic clusters are unique in that they make up a
474 sizeable fraction of particles at all sampling sites.

475 3.1.3. Inorganic Clusters (LDI, HDI1, HDI2, VHDI)

476 Other than C, N, O, and trace levels of Mg, no other elements are observed in the LDI cluster.
477 Carbon speciation, however, shows a clear inorganic core with an organic coating. This leaves only a few
478 options for the identity of the inorganic cores seen here. One possibility is that the inorganic core is
479 composed of elements not analyzed here, such as Si or Al. Due to the Al mounting plate and the Si(Li)
480 detector used, we are not able to quantitatively detect Al and Si. However, a more likely possibility is
481 that, as mentioned above, the inorganic cores that were initially detected with STXM were particularly
482 sensitive to electron beam damage leading to these sensitive inorganics (possibly ammonium sulfate)
483 being poorly characterized by EDX.

484 HDI1 is characterized by large, vaguely cubic, inorganic inclusions coated with organics. This
485 cluster has a fairly high fraction of O, Na, and Mg while containing the highest amount of Cl of any
486 cluster. The HD1 cluster is also unique in that particles in it were collected almost exclusively at the
487 ATTO site. Because of this, we suspect these particles represent marine aerosols [72-74]. [75]The organic
488 coating here is substantial and is likely due to aging as aerosols are transported inland to the ATTO site.
489 The transport of particles inland over a large distance is also reflected in the O/C ratio, where the particles
490 (specifically the organic coatings) may have oxidized more than other clusters.

491 HDI2 is characterized by many small inorganic inclusions speckled throughout the particles which
492 are not as localized as with the HDI1 cluster. There are small soot inclusions and an increased presence

493 of P, K, and S as compared to HDI1. These particles are mainly seen at the ZF2 site with a smaller portion
494 present at ATTO. Thus it is possible that this cluster is associated with spore rupturing but further
495 investigation is needed to apportion this cluster [75].

496 The VHDI cluster is unique in that it possesses the highest D_{α} value of any of the clusters at 4.83,
497 well above both the nominal “high diversity” value of 3.6 and the second highest D_{α} value of 3.83. This
498 cluster also has a large statistical error of 1.92 (at a 95% confidence level), which could indicate multiple
499 disparate groups are present in this cluster. This cluster is comprised mostly of particles from ZF2, but
500 ATTO and T3 particles contribute substantially as well. The VHDI cluster’s elemental composition is
501 similar to that of HDI2, but with a decreased C and O mass fraction and an enhancement of the other
502 elements, especially K (often seen in inorganic salt grains from biomass burning) [31,76]. Inorganics are
503 seen both as large localized inclusions, and as many small inclusions speckled throughout the particle.
504 This cluster’s high diversity and larger statistical spread may also be indicative of the varied biomass
505 burning fuels and burning conditions present.

506 3.1.4. Mixed Clusters (LDM, HDM)

507 The LDM cluster is characterized by all three carbon speciation types being present in many of the
508 particles. The presence of inorganic inclusions along with the lack of heavier elements suggests
509 ammonium nitrate (and possibly ammonium sulfate) as the identity of the inorganics. This cluster is seen
510 almost entirely at the ZF2 site which, along with its low diversity and few elemental constituents, may
511 indicate a local aerosol source near site ZF2. In which case, particles would have little time or distance to
512 age and scavenge new elements. The presence of soot in the LDM cluster might suggest these aerosols
513 come from the same source as the HDM cluster.

514 The species of carbon found in the HDM cluster’s particles are well mixed with soot, non-
515 carbonaceous inorganic, and organic carbon found in varying ratios. The large soot inclusions, high
516 diversity, and substantial presence of higher Z elements may point to an industrial or automotive origin.
517 Although the sizeable representation of the HDM cluster at T3 supports this, a slightly larger
518 representation is seen at site ZF2. This raises the possibility that some emissions from service vehicles
519 driving to or past the ZF2 site, or nearby generators may be collected at the ZF2 site. Emissions from
520 Manaus are not uncommon either and could account for this cluster’s presence at ZF2 [39].

521 3.1.5 Miscellaneous (Misc.) Clusters

522 Particles placed in this cluster were most likely grouped due to their supermicron size rather than
523 their composition or diversity. This cluster is comprised of some large rectangular crystals, particles
524 which did not fit well into the other clusters, as well as cases of particles with multiple large inclusions
525 (inorganic or soot) each encased within individual lobes. Since we could not include Al and Si in our
526 analysis, this cluster may also contain mineral dust particles (e.g. quartz and kaolinite) coated with
527 organic material.

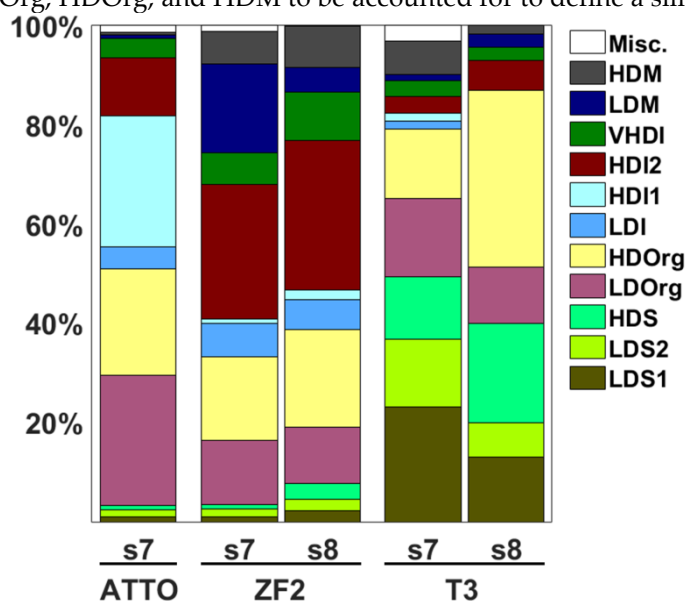
528 This last particle type may contain adjacent particles being erroneously deemed a single particle by
529 our detection algorithm because of overlap of the organic coating upon impaction. This grouping of
530 multiple individual particles into agglomerations much larger than expected for the given MOUDI stage
531 could have caused them to be placed in the Misc. cluster.

532 One notable particle type seen in this cluster is a collection of particles with a rectangular inorganic
533 core with a small patch of organic carbon in the center. Some of these inorganic cores wrap around the
534 carbon center while some others have a side missing but they all retain the same basic shape. The
535 elemental composition of the inorganic portion contains small amounts of Na and Mg, a relatively large
536 amount of S along with most of the particle’s N and O mass fraction. These particles are observed on the
537 only night time sample that was collected. This, along with the particles being found mainly at site T3

538 could suggest an industrial process whose emissions become easier to identify at night when other
 539 sources of aerosols (automotive) experience a decrease. Fragments of ruptured biological particles also
 540 may be a possibility based on their elemental composition [75].

541 3.2. Cluster Type Dependence on Sampling Site:

542 The cluster contributions at each sampling site are shown in Figure 5 separated by stage. Although
 543 particles from all cluster types were seen at each location, some particle types were predominantly
 544 associated with a particular sampling site. The clusters labeled LDOrg, HDOrg, HDI1, and HDI2 account
 545 for ~86% of the particles seen at the ATTO site. To account for a similar share of particles at site ZF2 one
 546 must consider the clusters labeled: HDI2, VHDI, LDOrg, HDOrg, LDM, and HDM. Site T3 requires
 547 LDS1, LDS2, HDS, LDOrg, HDOrg, and HDM to be accounted for to define a similar portion of particles.



548 **Figure 5.** Contribution of the twelve particle-type clusters identified in the samples from stage 7 (nominal
 549 aerodynamic size range: 560-320 nm) and stage 8 (320-180 nm) at each sampling site.

550 As the ATTO sampling site is less polluted and representative of biogenic aerosols, the presence of
 551 both organic clusters as well as two inorganic clusters with possible biogenic origins is expected.
 552 Conversely the relative absence of soot clusters or the mixed clusters further highlights the ATTO site's
 553 remoteness from regional anthropogenic (urban) influences. However, even this site is far from being
 554 pristine, as shown by the presence of significant amounts of BC, presumably from long-range transport.

555 While the ZF2 site contains many of the same clusters present at the ATTO site, there are some
 556 notable differences. The presence of the HDI1 cluster is diminished (~1% as compared to ATTO's 26%),
 557 and both mixed clusters are seen in substantial amounts. The largest difference between the two stages is
 558 the enhancement of the LDM cluster in stage 7 data and the minor increase in all three soot clusters in
 559 stage 8 particles.

560 Site T3 shows the presence of many clusters, with all three soot clusters present in substantial
 561 amounts. This is expected, as automotive exhaust or energy production through fuel oil burning will
 562 produce soot particles that travel to site T3 [77]. Both organic clusters are present with a slight
 563 enhancement in stage 8 particles. Because both organic clusters are seen in reasonable amounts at each
 564 sampling site, these particles may be part of the aerosol background inherent to sampling in a heavily

565 forested region. Stage 8 particles are also devoid of LDI, HDI1, and Misc. clusters, but few of these were
 566 seen in stage 7 and so this absence may be due to insufficient sampling.

567 Another aspect of Figure 5 is how many clusters make up most of each site's aerosol population, for
 568 which we use the following metric. Each site's cluster contribution is sorted in descending order and an
 569 effective number of clusters is found using $E(r) = \sum r f_r$, where r is the rank of each cluster's
 570 contribution to that site's population (with 1 assigned to the cluster with the largest contribution), f_r is the
 571 fraction of that site's population that cluster r accounts for, and $E(r)$ is the effective number of clusters.
 572 This metric will vary, in this case from 1 to 12, where the lower the effective number of clusters, the better
 573 a given site is characterized by fewer clusters. The values calculated from this metric are listed in Table 4.
 574 This metric highlights the increased diversity of sites T3 and ZF2 with respect to the ATTO site. Site
 575 ZF2's cluster composition is more varied. This is possibly due to specific events occurring during
 576 sampling, or by virtue of being closer to Manaus and therefore more susceptible to anthropogenic
 577 emissions. Site ZF2 samples were also collected over multiple days meaning some of the cluster
 578 variability may be due to the inclusion of both day and nighttime aerosols. This higher cluster variety
 579 could also be attributed to a local aerosol source as mentioned previously. Site T3 stage 7 shows the
 580 highest cluster variability due to T3's proximity to (and location downwind of) the anthropogenic center
 581 of Manaus. Stage 8 of site T3, in contrast, shows the lowest cluster variability. This may be the influence
 582 of fresh emissions coming from Manaus, which tend to be smaller in size and similar in composition
 583 (placing many of them in the same cluster).

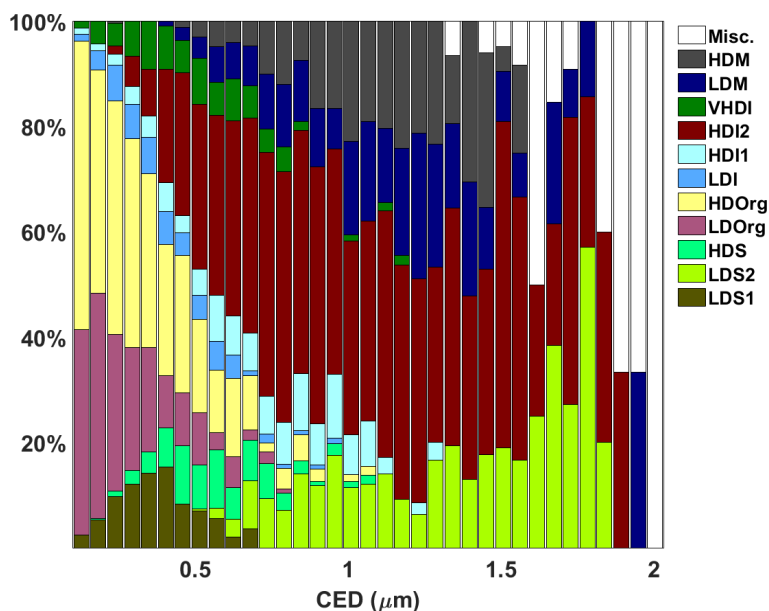
584 **Table 4.** Effective number of clusters for the available sampling site and stage data. The lower the value,
 585 the fewer clusters needed to characterize a majority of the sample.

	ATT O	ZF 2	T3
Stage 7	2.90	3.4	3.8
Stage 8	-	3.3	2.8
		7	6

586 3.3. Cluster Size Dependence:

587 Although relatively few supermicron particles were collected, most clusters included some fraction
 588 of both sub- and supermicron particles. Only 1 cluster (Misc) was exclusively supermicron in size
 589 whereas three clusters (LDS1, LDI, LDOrg) included exclusively submicron particles. Referencing Figure
 590 6, the only clusters observed in the supermicron size range were those labeled: Misc (located around 2
 591 μm with a very small percentage), LDM, HDM, HDI2, LDS2, and HDI1. Supermicron particles in the
 592 clusters HDS, HDOrg, and VHDI particles were also observed, but in very small numbers. Many clusters
 593 that make up the supermicron range represent more aged species.

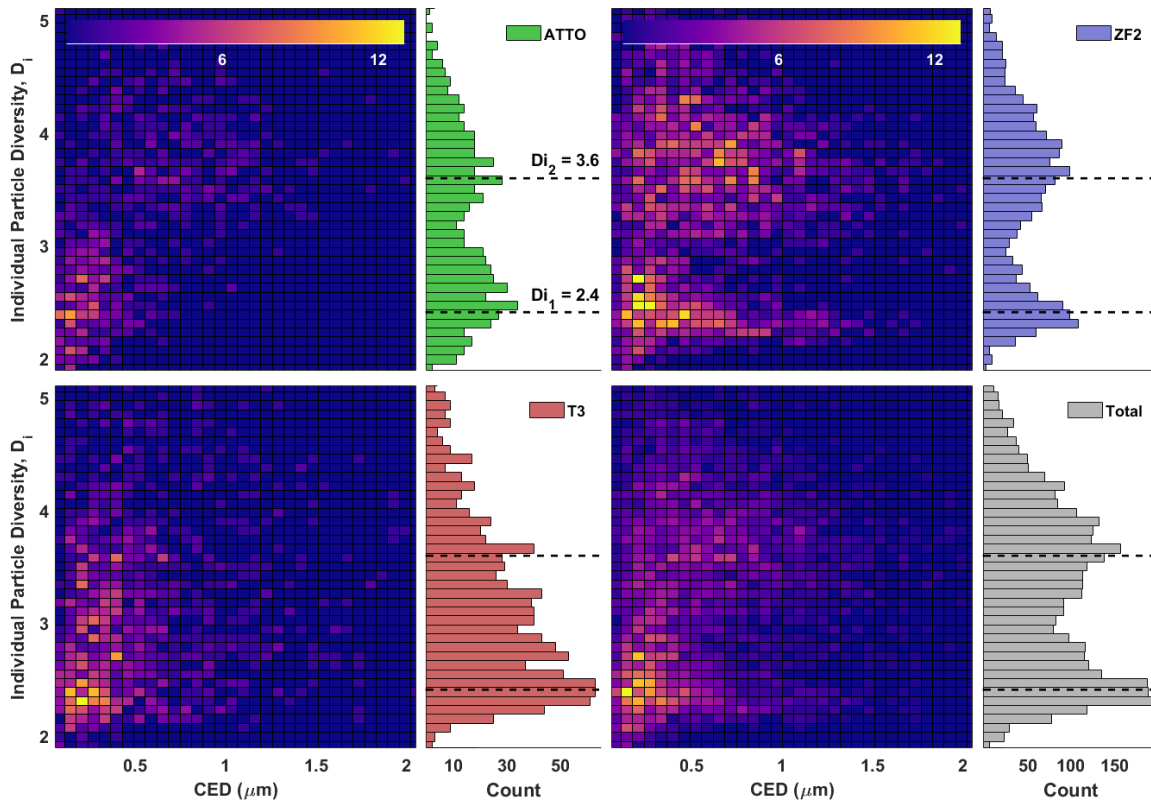
594 The submicron range is composed of many more clusters relative to the supermicron range. Many
 595 clusters in the submicron range were often labeled as less aged than the ones found in the supermicron
 596 range. This qualitative observation is supported by Figure 7 where there is an increasing trend in
 597 individual particle diversity (D_α) with increasing particle size and the notion that D_α is correlated with the
 598 extent of particle aging.



599 **Figure 6.** Cluster contribution for varying particle size. Particles $>2 \mu\text{m}$ have been omitted due to their
 600 very small abundance and to highlight submicron cluster composition.

601 3.4. *Composition and Diversity Size Dependence:*

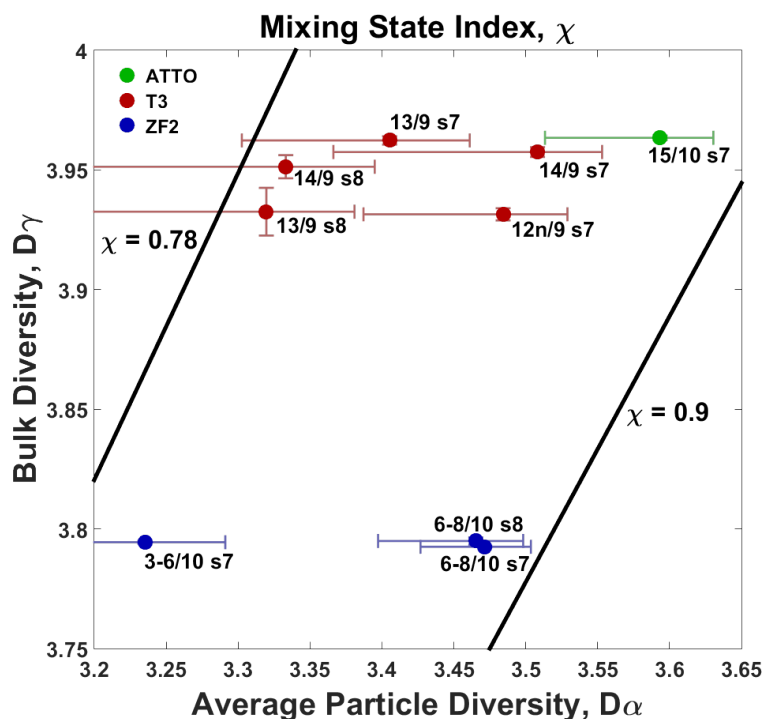
602 Submicron particles, as seen in Figure 7, have a high fraction of C, N, and O. With D_α values,
 603 calculated for both sub- and supermicron particles being 3.3 and 3.4 respectively, submicron particles
 604 appear to be the least diverse. However, the error analysis described below, renders this merely
 605 suggestive rather than conclusive. As particle size increases, two things are observed: 1) average particle
 606 diversity increases slightly and 2) the fraction of inorganics increases. Because of the ubiquity of C, N,
 607 and O in aerosol particles, the average particle diversity will almost always be slightly above 3. Given the
 608 relatively constant ratios of C, N, and O (with $O/C \approx 0.91$ and $N/C \approx 0.22$), individual particle diversity is
 609 not dependent on these elements; with the exception of soot. Rather, it is mainly the presence of heavier
 610 elements which are responsible for any increase in diversity. These larger particles, often represented by
 611 more aged clusters like LDS2, HDM, or HDI1, have had sufficient time and travel distance to acquire
 612 additional elements during the aging process. A similar conclusion was observed during the
 613 Carbonaceous Aerosol and Radiative Effects Study (CARES) conducted in 2010 in California, where
 614 heavier elements appreciably affected the mixing state of particles and increased with size, while C, N,
 615 and O remained constant [26,38].



642 **Figure 8.** Histograms of individual particle diversity values for each sampling site and the combined data
 643 set of all three sites. The individual diversity values for the two modes are indicated with dashed lines
 644 and were calculated by fitting two Gaussian distributions to the total data set histogram. Bin counts for
 645 2D histograms are represented by color values shown at the top.

646 *3.6. Mixing State of Particles at Different Sampling Sites:*

647 Entropy metrics were used to quantify mixing state for each sample analyzed here. Figure 9 shows
 648 the mixing state index (χ) corresponding to particles in each sample. In this case, the variation in mixing
 649 state index is small, with all samples having a χ bounded between 0.8 and 0.9. This is a result of D_α and
 650 D_γ consistently being around 3.4 and 3.9 respectively.



651 **Figure 9** Mixing state index of each sample (color coded by site) with associated error bars, adjusted to
 652 one-tenth of their size for readability. All average particle diversities are not significantly different. The
 653 site ZF2 bulk diversities are significantly different from the T3 and ATTO bulk diversities. Samples are
 654 labeled with day/month and stage number. The horizontal and vertical axes are essentially the numerator
 655 and denominator of the definition of χ (refer to Equation 14).

656 In the previous study by O'Brien et al. [26], similar sets of STXM and SEM/EDX data were collected
 657 for the CARES field campaign. In that study, the same diversity and mixing state parameterization was
 658 used except that STXM data (elements C, N, and O) and SEM/EDX (elements Na, Mg, S, P, Cl, K, Fe, Zn,
 659 Al, Si, Mn, and Ca) data were analyzed independently. They found that mixing state index values for
 660 heavier elements usually ranged from 0.4 – 0.6 with some values as high as 0.9. The values of χ for C, N,
 661 and O generally ranged from 0.75 to 0.9. The mixing state indices retrieved exclusively from STXM data
 662 closely matches the values determined in this paper. This suggests that χ is almost entirely determined
 663 by C, N, and O due to these three elements dominating the mass of the individual particles and the
 664 sample as a whole.

665 A point of note is the small spread of D_γ values within a given sampling site. With D_γ representing
 666 bulk diversity, these values serve to compare the average elemental composition (for the 14 elements
 667 chosen) of all aerosols, condensed down into one number. For a given site, samples analyzed were taken
 668 during the same season of the same year with similar wind trajectories, sampling times and sampling
 669 duration. It is expected then, that there will be a consistency in how much of any given element is
 670 present in the aerosol population, based on how much of each element is emitted and included in the
 671 particulate material. For D_γ to vary wildly from one day to another, or from one sampling period to
 672 another, would require an event or aerosol source producing substantially more of one element than
 673 usual.

674 The spread in D_α values among samples within a sampling site is much wider than that of D_γ . A
 675 large spread in D_α is expected when a singular diversity value is calculated from samples containing the
 676 variety of distinct particle types seen in Figure 3. This value is more susceptible to change from one

677 sampling date to another compared to D_{γ} and depends on how much of each aerosol type is collected
678 during a given sampling time.

679 The increase in the average particle diversity (D_{α}) with respect to increasing particle size is hinted at
680 here, albeit in less certain terms. Focusing on samples collected where both stage 7 and 8 data were
681 analyzed, average D_{α} values appear to be larger for stage 7 particles.

682 Samples collected at site T3 were expected to have a lower mixing state than either the ATTO or the
683 ZF2 site. This hypothesis was borne from the quantity of fresh emissions in Manaus, specifically soot
684 production from combustion, which would serve to drive the mixing state downwards towards total
685 external mixing. However, the end result of the error calculations in section 2.7 is that the values of χ for
686 each point in Figure 8a become statistically unresolvable as can be seen from the large error bars. This is
687 also not an issue that would be solved with any reasonable amount of extra data collection but is instead
688 mainly the consequence of the intrinsic spread in D_{α} .

689 4. Conclusions:

690 Presented here is a quantitative combination between two complementary per-particle
691 spectromicroscopy techniques, STXM/NEXAFS and SEM/EDX, on the exact same data set.
692 STXM/NEXAFS data was collected at the C, N, and O K-edges on a sub-particle level. This allowed not
693 only the quantitative determination of C, N, and O absolute masses, but also carbon speciation and
694 morphology. SEM/EDX allowed the approximate composition of the inorganic fraction to be determined
695 and then quantified along with the STXM data. The combination of these two techniques enables almost
696 all atmospherically relevant elements to be quantitatively probed on a per-particle basis. The potential
697 issue with S detection discussed above could be mitigated entirely in future measurements by conducting
698 STXM measurements at the S L-edge to obtain S mass fractions. This combined technique could be
699 especially useful for identifying aerosol sources using elemental tracers or unique elemental
700 compositions.

701 Using particle-specific elemental composition, size, carbon speciation, and individual particle
702 diversity (D_i), k-means clustering was used to separate particles into 12 clusters. The cluster average of
703 these same parameters allowed for potential sources to be assigned. It was found that the stage 7 of the
704 T3 site had a more varied population of particles (as defined by the effective cluster number) and
705 contained more soot-containing clusters than either the ATTO or ZF2 site. Clusters also exhibited size
706 dependence, with a large portion of supermicron particles assigned to high diversity clusters which have
707 been hypothesized to represent more aged particles. This approach could be used for even larger data
708 sets, especially those located at long-standing measurement facilities. From this, diurnal, seasonal, or
709 yearly changes in the aerosol population could be monitored directly. Application of this combined
710 technique would be especially fruitful near large pollution sources, as these anthropogenic sources are
711 difficult to model without the size-resolved composition presented here [78]. The clustering presented
712 here offers an opportunity not only to classify particles but also to identify sources, which can be
713 invaluable in determining the effects of trade or environmental protection policies. The largest
714 detriments to the utility of this composite technique are the long analysis times needed and the
715 requirement for two separate instruments as well as beam time at a synchrotron light source.

716 Utilizing the composite data set to determine a quantitative mixing state index revealed that
717 particles at site T3 were more externally mixed than at the other two sites. Error analysis, however,
718 shows a fairly large uncertainty in the elemental mixing state for all samples, with statistical errors in χ
719 ranging from 0.3 to 0.8. These error estimates do show that when calculating mixing state by using the 14
720 elements listed here, mixing state values are close together and show most samples to be highly (between
721 80 and 90%) internally mixed. Size-dependent trends were also observed in individual particle diversity,
722 with larger particles being slightly more diverse (3.3 and 3.4 for sub and supermicron particles

723 respectively). This size-dependent trend in diversity was seen even more drastically within the fine
724 mode, with particles $< 0.5 \mu\text{m}$ having an average D_i value of around 2.4 and particles $> 0.5 \mu\text{m}$ having
725 about a 3.6 diversity value, with a much larger spread of diversity values for larger particles. This
726 difference may identify a separation between fresh and aged aerosols in terms of diversity. This result
727 and the experimental method could be useful for climate models, allowing an experimental mixing state
728 and size-resolved particle composition to be used rather than assumed to improve model performance
729 [79-81]. Even though this type of individual particle microscopy study is time consuming, regions that
730 are important to global climate models (such as the Amazon) may benefit from the improved accuracy of
731 an experimentally determined mixing state.

732 The quantitative mixing state index presented is a useful tool, but its utility can be readily expanded.
733 Two of the advantages that this combined spectromicroscopy technique has are the ability to identify
734 morphology both of the particles as a whole and of the constituents within the particle. Due to the
735 general nature of the mixing state parameterization, the mixing state index and its interpretation is
736 heavily dependent on what components were used. In this study, 14 elements were used, however the
737 omission or addition of just a few elements (especially abundant elements such as carbon) could
738 drastically alter the value of χ . Because of this, specifics about which parameters were used and how
739 relevant they are to the samples being studied must be examined before interpreting the value of χ . How
740 well mixed individual elements are also may have limited usefulness to modelers or in general. With the
741 exception of elemental carbon, mass fractions of specific elements (like nitrogen) are less chemically
742 relevant than the molecules or ions they may be found in (nitrate vs. ammonium for example). Future
743 work will build upon this composite technique to instead determine masses and a molecular mixing state
744 for chemically and atmospherically relevant species such as nitrate, carbonate, sulfate, and etc.
745 Modification in this way could allow our current combined technique to determine an aerosol
746 population's radiative forcing contribution due to both direct and indirect effects. Specific aspects about
747 the indirect effect like hygroscopicity or the number of effective Cloud Condensation Nuclei (CCN)
748 within a population of aerosols could also be gleaned from this method [82]. This type of modification
749 would bolster the usefulness of this technique as well as the usefulness of χ for climate modelers.

750 **Supplementary Materials:** The MatLab scripts used to analyze this data are available online at:
751 github.com/MFraund/ElementalMixingStateofAerosolsDuringGoamazon_2017. The following are available online at
752 www.mdpi.com/LINK, Figure S1: 72 hour back trajectories at varied starting elevations for each sample site

753 **Acknowledgements:** Funding for sample collection during GoAmazon2014/5 study was provided by the
754 Atmospheric Radiation Measurement Program sponsored by the U.S. Department of Energy (DOE), Office of Science,
755 Office of Biological and Environmental Research (OBER), Climate and Environmental Sciences Division (CESD).
756 Funding for the data analysis was provided by the U.S. DOE's Atmospheric System Research Program, BER under
757 grant DE-SC0013960. The STXM/NEXAFS particle analysis was performed at beamline 5.3.2.2 and at 11.0.2.2 at the
758 Advanced Light Source (ALS) at Lawrence Berkeley National Laboratory. The work at the ALS was supported by
759 the Director, Office of Science, Office of Basic Energy Sciences, of the U.S. DOE under contract DE-AC02-05CH11231.
760 We thank A.L.D. Kilcoyne, Young-Sang Yu, and David Shapiro for their assistance with STXM experiments. Data
761 were obtained from the Atmospheric Radiation Measurement (ARM) Program sponsored by the U.S. Department of
762 Energy, Office of Science, Office of Biological and Environmental Research, Climate and Environmental Sciences
763 Division The CCSEM/EDX analysis was performed at Environmental Molecular Sciences Laboratory, a National
764 Scientific User Facility sponsored by OBER at PNNL. PNNL is operated by the US Department of Energy by Battelle
765 Memorial Institute under contract DE-AC06-76RL0. This work has been supported by the Max Planck Society
766 (MPG). For the operation of the ATTO site, we acknowledge the support by the German Federal Ministry of
767 Education and Research (BMBF contract 01LB1001A) and the Brazilian Ministério da Ciência, Tecnologia e Inovação
768 (MCTI/FINEP contract 01.11.01248.00) as well as the Amazon State University (UEA), FAPEAM, LBA/INPA and
769 SDS/CEUC/RDS-Uatumã. This paper contains results of research conducted under the Technical/Scientific

770 Cooperation Agreement between the National Institute for Amazonian Research, the State University of Amazonas,
771 and the Max-Planck-Gesellschaft e.V.; the opinions expressed are the entire responsibility of the authors and not of
772 the participating institutions. We highly acknowledge the support by the Instituto Nacional de Pesquisas da
773 Amazônia (INPA). We would like to especially thank all the people involved in the technical, logistical, and scientific
774 support of the ATTO project. The authors gratefully acknowledge the NOAA Air Resources Laboratory (ARL) for the
775 provision of the HYSPLIT transport and dispersion model and/or READY website (<http://www.ready.noaa.gov>) used
776 in this publication. P. Artaxo acknowledges funding from FAPESP and CNPq. The work was conducted under
777 001030/2012-4 of the Brazilian National Council for Scientific and Technological Development (CNPq). The authors
778 thank Glauber Cirino for help in collecting samples at ZF2. The authors also thank Rachel O'Brien for her
779 participation in sample collection and Jost V. Lavric, Stefan Wolff, Jorge Saturno, and David Walter for providing
780 ATTO peripheral data and Luciana Rizzo for providing ZF2 peripheral data.

781 **Author Contributions:** M.F led data collection analysis and writing. D.Q.P. and D.B collected STXM data. T.H.H.
782 and B.W. collected STXM/SEM data and assisted with analysis. C.P. provided ATTO microscopy samples and ATTO
783 peripheral data. A.L. provided ZF2 samples. S.C. (PNNL) assisted in collecting SEM data. M.K.G. provided T3
784 samples and collected STXM/SEM data on samples. S.S.dS. and S.T.M. provided T3 supporting data. P.A. and S.C.
785 (USP) provided ZF2 supporting data. R.C.M. conceived the experiment, collected STXM data, and administered the
786 project. All authors provided input on the project and edited the manuscript.

787 **Conflicts of Interest:** The authors declare no conflict of interest. The founding sponsors had no role in the design of
788 the study; in the collection, analyses, or interpretation of data; in the writing of the manuscript, and in the decision to
789 publish the results

790 References

- 791 1. Seinfeld, J.H.; Pandis, S.N. *Atmospheric chemistry and physics: From air pollution to*
792 *climate change*. John Wiley & Sons: 2012.
- 793 2. Stocker, T.; Qin, D.; Plattner, G.; Tignor, M.; Allen, S.; Boschung, J.; Nauels, A.; Xia,
794 Y.; Bex, V.; Midgley, P. Contribution of working group I to the fifth assessment report of
795 the intergovernmental panel on climate change. *Climate Change* **2013**.
- 796 3. Pöschl, U. Atmospheric aerosols: Composition, transformation, climate and health
797 effects. *Angewandte Chemie International Edition* **2005**, *44*, 7520-7540.
- 798 4. Jacobson, M.Z. Strong radiative heating due to the mixing state of black carbon in
799 atmospheric aerosols. *Nature* **2001**, *409*, 695-697.
- 800 5. Moffet, R.C.; Prather, K.A. In-situ measurements of the mixing state and optical
801 properties of soot with implications for radiative forcing estimates. *Proceedings of the*
802 *National Academy of Sciences* **2009**, *106*, 11872-11877.
- 803 6. Fierce, L.; Riemer, N.; Bond, T.C. Explaining variance in black carbon's aging timescale.
804 *Atmospheric Chemistry and Physics* **2015**, *15*, 3173-3191.
- 805 7. Ault, A.P.; Axson, J.L. Atmospheric aerosol chemistry: Spectroscopic and microscopic
806 advances. *Analytical Chemistry* **2016**, *89*, 430-452.
- 807 8. Warren, D.R.; Seinfeld, J.H. Simulation of aerosol size distribution evolution in systems
808 with simultaneous nucleation, condensation, and coagulation. *Aerosol Science and*
809 *Technology* **1985**, *4*, 31-43.
- 810 9. Moffet, R.C.; Prather, K.A. In-situ measurements of the mixing state and optical
811 properties of soot with implications for radiative forcing estimates. *Proceedings of the*
812 *National Academy of Sciences of the United States of America* **2009**, *106*, 11872-11877.
- 813 10. Liu, D.; Whitehead, J.; Alfarra, M.R.; Reyes-Villegas, E.; Spracklen, D.V.; Reddington,
814 C.L.; Kong, S.; Williams, P.I.; Ting, Y.-C.; Haslett, S. Black-carbon absorption

- 815 enhancement in the atmosphere determined by particle mixing state. *Nature Geoscience*
816 **2017**, *10*, 184-188.
- 817 11. Peng, J.; Hu, M.; Guo, S.; Du, Z.; Zheng, J.; Shang, D.; Zamora, M.L.; Zeng, L.; Shao,
818 M.; Wu, Y.-S. Markedly enhanced absorption and direct radiative forcing of black carbon
819 under polluted urban environments. *Proceedings of the National Academy of Sciences*
820 **2016**, *113*, 4266-4271.
- 821 12. Raatikainen, T.; Brus, D.; Hyvärinen, A.-P.; Svensson, J.; Asmi, E.; Lihavainen, H. Black
822 carbon concentrations and mixing state in the Finnish Arctic. *Atmospheric Chemistry and*
823 *Physics* **2015**, *15*, 10057-10070.
- 824 13. D'Almeida, G.A.; Koepke, P.; Shettle, E.P. *Atmospheric aerosols: Global climatology*
825 *and radiative characteristics*. A Deepak Pub: 1991.
- 826 14. Cappa, C.D.; Onasch, T.B.; Massoli, P.; Worsnop, D.R.; Bates, T.S.; Cross, E.S.;
827 Davidovits, P.; Hakala, J.; Hayden, K.L.; Jobson, B.T. Radiative absorption
828 enhancements due to the mixing state of atmospheric black carbon. *Science* **2012**, *337*,
829 1078-1081.
- 830 15. Schmidt, G.A.; Ruedy, R.; Hansen, J.E.; Aleinov, I.; Bell, N.; Bauer, M.; Bauer, S.;
831 Cairns, B.; Canuto, V.; Cheng, Y. Present-day atmospheric simulations using GISS
832 modelE: Comparison to in situ, satellite, and reanalysis data. *Journal of Climate* **2006**,
833 *19*, 153-192.
- 834 16. Jacobson, M.Z. GATOR-GCMM: A global-through urban-scale air pollution and weather
835 forecast model: 1. Model design and treatment of subgrid soil, vegetation, roads,
836 rooftops, water, sea ice, and snow. *Journal of Geophysical Research: Atmospheres* **2001**,
837 *106*, 5385-5401.
- 838 17. Zaveri, R.A.; Barnard, J.C.; Easter, R.C.; Riemer, N.; West, M. Particle-resolved
839 simulation of aerosol size, composition, mixing state, and the associated optical and
840 cloud condensation nuclei activation properties in an evolving urban plume. *Journal of*
841 *Geophysical Research: Atmospheres* **2010**, *115*.
- 842 18. Schwarz, J.; Gao, R.; Fahey, D.; Thomson, D.; Watts, L.; Wilson, J.; Reeves, J.;
843 Darbeheshti, M.; Baumgardner, D.; Kok, G. Single-particle measurements of midlatitude
844 black carbon and light-scattering aerosols from the boundary layer to the lower
845 stratosphere. *Journal of Geophysical Research: Atmospheres* **2006**, *111*.
- 846 19. Sedlacek, A.J.; Lewis, E.R.; Kleinman, L.; Xu, J.; Zhang, Q. Determination of and
847 evidence for non-core-shell structure of particles containing black carbon using the
848 single-particle soot photometer (SP2). *Geophysical Research Letters* **2012**, *39*.
- 849 20. Healy, R.M.; Riemer, N.; Wenger, J.C.; Murphy, M.; West, M.; Poulain, L.;
850 Wiedensohler, A.; O'Connor, I.P.; McGillicuddy, E.; Sodeau, J.R. Single particle
851 diversity and mixing state measurements. *Atmospheric Chemistry and Physics* **2014**, *14*,
852 6289-6299.
- 853 21. Riemer, N.; West, M. Quantifying aerosol mixing state with entropy and diversity
854 measures. *Atmospheric Chemistry and Physics* **2013**, *13*, 11423-11439.
- 855 22. Hopkins, R.J.; Tivanski, A.V.; Marten, B.D.; Gilles, M.K. Chemical bonding and
856 structure of black carbon reference materials and individual carbonaceous atmospheric
857 aerosols. *Journal of Aerosol Science* **2007**, *38*, 573-591.
- 858 23. Moffet, R.C. Scanning transmission x-ray microscopy: Applications in atmospheric
859 aerosol research. *Lawrence Berkeley National Laboratory* **2011**.

- 860 24. Laskin, A.; Cowin, J.P.; Iedema, M.J. Analysis of individual environmental particles
861 using modern methods of electron microscopy and x-ray microanalysis. *Journal of*
862 *Electron Spectroscopy and Related Phenomena* **2006**, *150*, 260-274.
- 863 25. Falcone, R.; Sommariva, G.; Verità, M. WDXRF, EPMA and SEM/EDX quantitative
864 chemical analyses of small glass samples. *Microchimica Acta* **2006**, *155*, 137-140.
- 865 26. O'Brien, R.E.; Wang, B.; Laskin, A.; Riemer, N.; West, M.; Zhang, Q.; Sun, Y.; Yu,
866 X.Y.; Alpert, P.; Knopf, D.A. Chemical imaging of ambient aerosol particles:
867 Observational constraints on mixing state parameterization. *Journal of Geophysical*
868 *Research: Atmospheres* **2015**, *120*, 9591-9605.
- 869 27. Piens, D.S.; Kelly, S.T.; Harder, T.H.; Petters, M.D.; O'Brien, R.E.; Wang, B.; Teske, K.;
870 Dowell, P.; Laskin, A.; Gilles, M.K. Measuring mass-based hygroscopicity of
871 atmospheric particles through in situ imaging. *Environ. Sci. Technol* **2016**, *50*, 5172-
872 5180.
- 873 28. Streets, D.; Bond, T.; Lee, T.; Jang, C. On the future of carbonaceous aerosol emissions.
874 *Journal of Geophysical Research: Atmospheres* **2004**, *109*.
- 875 29. Artaxo, P.; Rizzo, L.V.; Brito, J.F.; Barbosa, H.M.; Arana, A.; Sena, E.T.; Cirino, G.G.;
876 Bastos, W.; Martin, S.T.; Andreae, M.O. Atmospheric aerosols in Amazonia and land use
877 change: From natural biogenic to biomass burning conditions. *Faraday discussions* **2013**,
878 *165*, 203-235.
- 879 30. Wang, J.; Krejci, R.; Giangrande, S.; Kuang, C.; Barbosa, H.M.; Brito, J.; Carbone, S.;
880 Chi, X.; Comstock, J.; Ditas, F. Amazon boundary layer aerosol concentration sustained
881 by vertical transport during rainfall. *Nature* **2016**, *539*, 416-419.
- 882 31. Martin, S.T.; Andreae, M.O.; Artaxo, P.; Baumgardner, D.; Chen, Q.; Goldstein, A.H.;
883 Guenther, A.; Heald, C.L.; Mayol-Bracero, O.L.; McMurry, P.H. Sources and properties
884 of Amazonian aerosol particles. *Reviews of Geophysics* **2010**, *48*.
- 885 32. Bond, T.; Venkataraman, C.; Maser, O. Global atmospheric impacts of residential fuels.
886 *Energy for Sustainable Development* **2004**, *8*, 20-32.
- 887 33. Staudt, A.; Jacob, D.J.; Logan, J.A.; Bachiochi, D.; Krishnamurti, T.; Sachse, G.
888 Continental sources, transoceanic transport, and interhemispheric exchange of carbon
889 monoxide over the Pacific. *Journal of Geophysical Research: Atmospheres* **2001**, *106*,
890 32571-32589.
- 891 34. Kuhn, U.; Ganzeveld, L.; Thielmann, A.; Dindorf, T.; Schebeske, G.; Welling, M.;
892 Sciare, J.; Roberts, G.; Meixner, F.; Kesselmeier, J. Impact of Manaus city on the
893 Amazon green ocean atmosphere: Ozone production, precursor sensitivity and aerosol
894 load. *Atmospheric Chemistry and Physics* **2010**, *10*, 9251-9282.
- 895 35. Martin, S.; Artaxo, P.; Machado, L.; Manzi, A.; Souza, R.; Schumacher, C.; Wang, J.;
896 Andreae, M.; Barbosa, H.; Fan, J. Introduction: Observations and modeling of the green
897 ocean Amazon (GoAmazon2014/5). *Atmospheric Chemistry and Physics* **2016**, *16*, 4785-
898 4797.
- 899 36. Martin, S.T.; Artaxo, P.; Machado, L.; Manzi, A.; Souza, R.; Schumacher, C.; Wang, J.;
900 Biscaro, T.; Brito, J.; Calheiros, A. The green ocean Amazon experiment
901 (GoAmazon2014/5) observes pollution affecting gases, aerosols, clouds, and rainfall over
902 the rain forest. *Bulletin of the American Meteorological Society* **2017**, *98*, 981-997.
- 903 37. Swap, R.; Garstang, M.; Greco, S.; Talbot, R.; Kållberg, P. Saharan dust in the Amazon
904 Basin. *Tellus B* **1992**, *44*, 133-149.

- 905 38. Pöschl, U.; Martin, S.; Sinha, B.; Chen, Q.; Gunthe, S.; Huffman, J.; Borrmann, S.;
906 Farmer, D.; Garland, R.; Helas, G. Rainforest aerosols as biogenic nuclei of clouds and
907 precipitation in the Amazon. *science* **2010**, *329*, 1513-1516.
- 908 39. Martin, S.; Andreae, M.; Althausen, D.; Artaxo, P.; Baars, H.; Borrmann, S.; Chen, Q.;
909 Farmer, D.; Guenther, A.; Gunthe, S. An overview of the Amazonian aerosol
910 characterization experiment 2008 (amaze-08). *Atmospheric Chemistry and Physics* **2010**,
911 *10*.
- 912 40. Chen, Q.; Farmer, D.; Rizzo, L.; Pauliquevis, T.; Kuwata, M.; Karl, T.G.; Guenther, A.;
913 Allan, J.D.; Coe, H.; Andreae, M. Submicron particle mass concentrations and sources in
914 the Amazonian wet season (AMAZE-08). *Atmospheric Chemistry and Physics* **2015**, *15*,
915 3687-3701.
- 916 41. Andreae, M.; Acevedo, O.; Araùjo, A.; Artaxo, P.; Barbosa, C.; Barbosa, H.; Brito, J.;
917 Carbone, S.; Chi, X.; Cintra, B. The Amazon Tall Tower Observatory (ATTO): Overview
918 of pilot measurements on ecosystem ecology, meteorology, trace gases, and aerosols.
919 *Atmospheric Chemistry and Physics* **2015**, *15*, 10723-10776.
- 920 42. Stein, A.; Draxler, R.R.; Rolph, G.D.; Stunder, B.J.; Cohen, M.; Ngan, F. NOAA's
921 HYSPLIT atmospheric transport and dispersion modeling system. *Bulletin of the*
922 *American Meteorological Society* **2015**, *96*, 2059-2077.
- 923 43. Rolph, G.; Stein, A.; Stunder, B. Real-time environmental applications and display
924 system: Ready. *Environmental Modelling & Software* **2017**, *95*, 210-228.
- 925 44. Kilcoyne, A.; Tyliszczak, T.; Steele, W.; Fakra, S.; Hitchcock, P.; Franck, K.; Anderson,
926 E.; Harteneck, B.; Rightor, E.; Mitchell, G. Interferometer-controlled scanning
927 transmission x-ray microscopes at the Advanced Light Source. *Journal of synchrotron*
928 *radiation* **2003**, *10*, 125-136.
- 929 45. Henke, B.L.; Gullikson, E.M.; Davis, J.C. X-ray interactions: Photoabsorption, scattering,
930 transmission, and reflection at $e= 50$ -30,000 eV, $z= 1$ -92. *Atomic data and nuclear data*
931 *tables* **1993**, *54*, 181-342.
- 932 46. Moffet, R.C.; Henn, T.; Laskin, A.; Gilles, M.K. Automated chemical analysis of
933 internally mixed aerosol particles using x-ray spectromicroscopy at the carbon K-edge†.
934 *Analytical chemistry* **2010**, *82*, 7906-7914.
- 935 47. Guizar-Sicairos, M.; Thurman, S.T.; Fienup, J.R. Efficient subpixel image registration
936 algorithms. *Optics letters* **2008**, *33*, 156-158.
- 937 48. Otsu, N. A threshold selection method from gray-level histograms. *Automatica* **1975**, *11*,
938 23-27.
- 939 49. Artaxo, P.; Martins, J.V.; Yamasoe, M.A.; Procópio, A.S.; Pauliquevis, T.M.; Andreae,
940 M.O.; Guyon, P.; Gatti, L.V.; Leal, A.M.C. Physical and chemical properties of aerosols
941 in the wet and dry seasons in Rondônia, Amazonia. *Journal of Geophysical Research:*
942 *Atmospheres* **2002**, *107*.
- 943 50. Hartigan, J.A.; Wong, M.A. Algorithm as 136: A k-means clustering algorithm. *Journal*
944 *of the Royal Statistical Society. Series C (Applied Statistics)* **1979**, *28*, 100-108.
- 945 51. Rebotier, T.P.; Prather, K.A. Aerosol time-of-flight mass spectrometry data analysis: A
946 benchmark of clustering algorithms. *Analytica chimica acta* **2007**, *585*, 38-54.
- 947 52. Kodinariya, T.M.; Makwana, P.R. Review on determining number of cluster in k-means
948 clustering. *International Journal* **2013**, *1*, 90-95.
- 949 53. de Sá, S.S.; Palm, B.B.; Campuzano-Jost, P.; Day, D.A.; Newburn, M.K.; Hu, W.;
950 Isaacman-VanWertz, G.; Yee, L.D.; Thalman, R.; Brito, J., *et al.* Influence of urban

- 951 pollution on the production of organic particulate matter from isoprene epoxydiols in
952 central Amazonia. *Atmos. Chem. Phys.* **2017**, *17*, 6611-6629.
- 953 54. Kirkman, G.; Gut, A.; Ammann, C.; Gatti, L.; Cordova, A.; Moura, M.; Andreae, M.;
954 Meixner, F. Surface exchange of nitric oxide, nitrogen dioxide, and ozone at a cattle
955 pasture in Rondonia, Brazil. *Journal of Geophysical Research: Atmospheres* **2002**, *107*.
956 55. Ahlm, L.; Nilsson, E.; Krejci, R.; Mårtensson, E.; Vogt, M.; Artaxo, P. A comparison of
957 dry and wet season aerosol number fluxes over the Amazon rain forest. *Atmospheric*
958 *Chemistry & Physics Discussions* **2009**, *9*.
- 959 56. Saturno, J.; Pöhlker, C.; Massabò, D.; Brito, J.; Carbone, S.; Cheng, Y.; Chi, X.; Ditas,
960 F.; de Angelis, I.H.; Morán-Zuloaga, D. Comparison of different aethalometer correction
961 schemes and a reference multi-wavelength absorption technique for ambient aerosol data.
962 *Atmospheric Measurement Techniques* **2017**, *10*, 2837.
- 963 57. Li, J.; Pósfai, M.; Hobbs, P.V.; Buseck, P.R. Individual aerosol particles from biomass
964 burning in southern Africa: 2, compositions and aging of inorganic particles. *Journal of*
965 *Geophysical Research: Atmospheres* **2003**, *108*.
- 966 58. Ault, A.P.; Moffet, R.C.; Baltrusaitis, J.; Collins, D.B.; Ruppel, M.J.; Cuadra-Rodriguez,
967 L.A.; Zhao, D.; Guasco, T.L.; Ebben, C.J.; Geiger, F.M. Size-dependent changes in sea
968 spray aerosol composition and properties with different seawater conditions.
969 *Environmental science & technology* **2013**, *47*, 5603-5612.
- 970 59. Pöhlker, C.; Wiedemann, K.T.; Sinha, B.; Shiraiwa, M.; Gunthe, S.S.; Smith, M.; Su, H.;
971 Artaxo, P.; Chen, Q.; Cheng, Y. Biogenic potassium salt particles as seeds for secondary
972 organic aerosol in the Amazon. *Science* **2012**, *337*, 1075-1078.
- 973 60. Brooks, S.D.; Garland, R.M.; Wise, M.E.; Prenni, A.J.; Cushing, M.; Hewitt, E.; Tolbert,
974 M.A. Phase changes in internally mixed maleic acid/ammonium sulfate aerosols. *Journal*
975 *of Geophysical Research: Atmospheres* **2003**, *108*.
- 976 61. Pósfai, M.; Gelencsér, A.; Simonics, R.; Arató, K.; Li, J.; Hobbs, P.V.; Buseck, P.R.
977 Atmospheric tar balls: Particles from biomass and biofuel burning. *Journal of*
978 *Geophysical Research: Atmospheres* **2004**, *109*.
- 979 62. Artaxo, P.; Gerab, F.; Rabello, M.L. Elemental composition of aerosol particles from two
980 atmospheric monitoring stations in the Amazon Basin. *Nuclear Instruments and Methods*
981 *in Physics Research Section B: Beam Interactions with Materials and Atoms* **1993**, *75*,
982 277-281.
- 983 63. Artaxo, P.; Gerab, F.; Yamasoe, M.A.; Martins, J.V. Fine mode aerosol composition at
984 three long-term atmospheric monitoring sites in the Amazon Basin. *Journal of*
985 *Geophysical Research: Atmospheres* **1994**, *99*, 22857-22868.
- 986 64. Andreae, M.O. Soot carbon and excess fine potassium: Long-range transport of
987 combustion-derived aerosols. *Science* **1983**, *220*, 1148-1151.
- 988 65. Maudlin, L.; Wang, Z.; Jonsson, H.; Sorooshian, A. Impact of wildfires on size-resolved
989 aerosol composition at a coastal California site. *Atmospheric Environment* **2015**, *119*, 59-
990 68.
- 991 66. Wonaschütz, A.; Hersey, S.; Sorooshian, A.; Craven, J.; Metcalf, A.; Flagan, R.;
992 Seinfeld, J. Impact of a large wildfire on water-soluble organic aerosol in a major urban
993 area: The 2009 station fire in Los Angeles county. *Atmospheric Chemistry and Physics*
994 **2011**, *11*, 8257-8270.
- 995 67. Rudich, Y.; Donahue, N.M.; Mentel, T.F. Aging of organic aerosol: Bridging the gap
996 between laboratory and field studies. *Annu. Rev. Phys. Chem.* **2007**, *58*, 321-352.

- 997 68. Zhang, R.; Khalizov, A.F.; Pagels, J.; Zhang, D.; Xue, H.; McMurry, P.H. Variability in
998 morphology, hygroscopicity, and optical properties of soot aerosols during atmospheric
999 processing. *Proceedings of the National Academy of Sciences* **2008**, *105*, 10291-10296.
- 1000 69. Soto-Garcia, L.L.; Andreae, M.O.; Andreae, T.W.; Artaxo, P.; Maenhaut, W.;
1001 Kirchstetter, T.; Novakov, T.; Chow, J.C.; Mayol-Bracero, O.L. Evaluation of the carbon
1002 content of aerosols from the burning of biomass in the Brazilian Amazon using thermal,
1003 optical and thermal-optical analysis methods. *Atmospheric Chemistry and Physics* **2011**,
1004 *11*, 4425-4444.
- 1005 70. Sorooshian, A.; Crosbie, E.; Maudlin, L.C.; Youn, J.S.; Wang, Z.; Shingler, T.; Ortega,
1006 A.M.; Hersey, S.; Woods, R.K. Surface and airborne measurements of organosulfur and
1007 methanesulfonate over the western United States and coastal areas. *Journal of*
1008 *Geophysical Research: Atmospheres* **2015**, *120*, 8535-8548.
- 1009 71. Aiken, A.C.; Decarlo, P.F.; Kroll, J.H.; Worsnop, D.R.; Huffman, J.A.; Docherty, K.S.;
1010 Ulbrich, I.M.; Mohr, C.; Kimmel, J.R.; Sueper, D. O/C and OM/OC ratios of primary,
1011 secondary, and ambient organic aerosols with high-resolution time-of-flight aerosol mass
1012 spectrometry. *Environmental Science & Technology* **2008**, *42*, 4478-4485.
- 1013 72. Artaxo, P.; Storms, H.; Bruynseels, F.; Van Grieken, R.; Maenhaut, W. Composition and
1014 sources of aerosols from the Amazon Basin. *Journal of Geophysical Research:*
1015 *Atmospheres* **1988**, *93*, 1605-1615.
- 1016 73. Garstang, M.; Greco, S.; Scala, J.; Swap, R.; Ulanski, S.; Fitzjarrald, D.; Martin, D.;
1017 Browell, E.; Shipman, M.; Connors, V. The Amazon boundary-layer experiment (ABLE
1018 2B): A meteorological perspective. *Bulletin of the American Meteorological Society*
1019 **1990**, *71*, 19-32.
- 1020 74. Artaxo, P.; Fernandes, E.T.; Martins, J.V.; Yamasoe, M.A.; Hobbs, P.V.; Maenhaut, W.;
1021 Longo, K.M.; Castanho, A. Large-scale aerosol source apportionment in Amazonia.
1022 *Journal of Geophysical Research: Atmospheres* **1998**, *103*, 31837-31847.
- 1023 75. China, S.; Wang, B.; Weis, J.; Rizzo, L.; Brito, J.; Cirino, G.G.; Kovarik, L.; Artaxo, P.;
1024 Gilles, M.K.; Laskin, A. Rupturing of biological spores as a source of secondary particles
1025 in Amazonia. *Environmental Science & Technology* **2016**, *50*, 12179-12186.
- 1026 76. Pósfai, M.; Simonics, R.; Li, J.; Hobbs, P.V.; Buseck, P.R. Individual aerosol particles
1027 from biomass burning in southern Africa: 1. Compositions and size distributions of
1028 carbonaceous particles. *Journal of Geophysical Research: Atmospheres* **2003**, *108*.
- 1029 77. Colbeck, I.; Atkinson, B.; Johar, Y. The morphology and optical properties of soot
1030 produced by different fuels. *Journal of aerosol science* **1997**, *28*, 715-723.
- 1031 78. Ervens, B.; Cubison, M.; Andrews, E.; Feingold, G.; Ogren, J.; Jimenez, J.; Quinn, P.;
1032 Bates, T.; Wang, J.; Zhang, Q. Ccn predictions using simplified assumptions of organic
1033 aerosol composition and mixing state: A synthesis from six different locations.
1034 *Atmospheric Chemistry and Physics* **2010**, *10*, 4795-4807.
- 1035 79. Medina, J.; Nenes, A.; Sotiropoulou, R.E.P.; Cottrell, L.D.; Ziemba, L.D.; Beckman, P.J.;
1036 Griffin, R.J. Cloud condensation nuclei closure during the international consortium for
1037 atmospheric research on transport and transformation 2004 campaign: Effects of size-
1038 resolved composition. *Journal of Geophysical Research: Atmospheres* **2007**, *112*.
- 1039 80. Cubison, M.; Ervens, B.; Feingold, G.; Docherty, K.; Ulbrich, I.; Shields, L.; Prather, K.;
1040 Hering, S.; Jimenez, J. The influence of chemical composition and mixing state of Los
1041 Angeles urban aerosol on CCN number and cloud properties. *Atmospheric Chemistry and*
1042 *Physics* **2008**, *8*, 5649-5667.

- 1043 81. Stroud, C.A.; Nenes, A.; Jimenez, J.L.; DeCarlo, P.F.; Huffman, J.A.; Bruintjes, R.;
1044 Nemitz, E.; Delia, A.E.; Toohey, D.W.; Guenther, A.B. Cloud activating properties of
1045 aerosol observed during CELTIC. *Journal of the atmospheric sciences* **2007**, *64*, 441-
1046 459.
- 1047 82. Wang, J.; Cubison, M.; Aiken, A.; Jimenez, J.; Collins, D. The importance of aerosol
1048 mixing state and size-resolved composition on CCN concentration and the variation of
1049 the importance with atmospheric aging of aerosols. *Atmospheric Chemistry and Physics*
1050 **2010**, *10*, 7267-7283.

1051 © 2017 by the authors. Submitted for possible open access publication under the
1052 terms and conditions of the Creative Commons Attribution (CC BY) license
1053 (<http://creativecommons.org/licenses/by/4.0/>).
1054

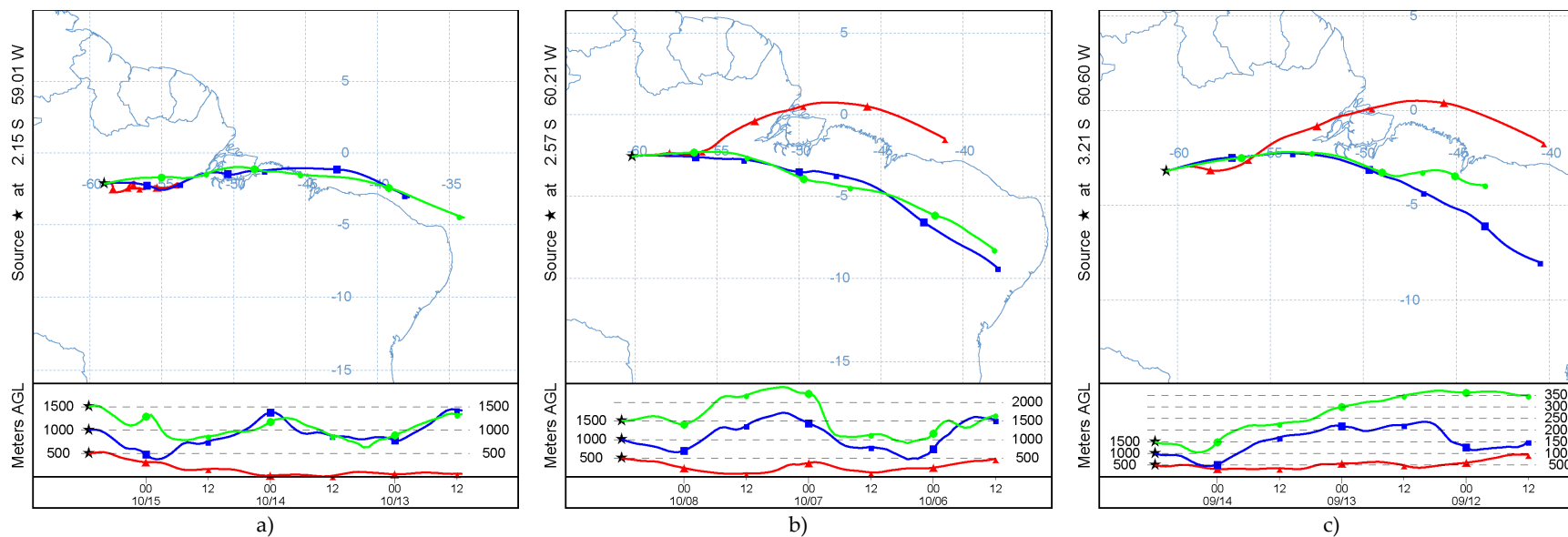
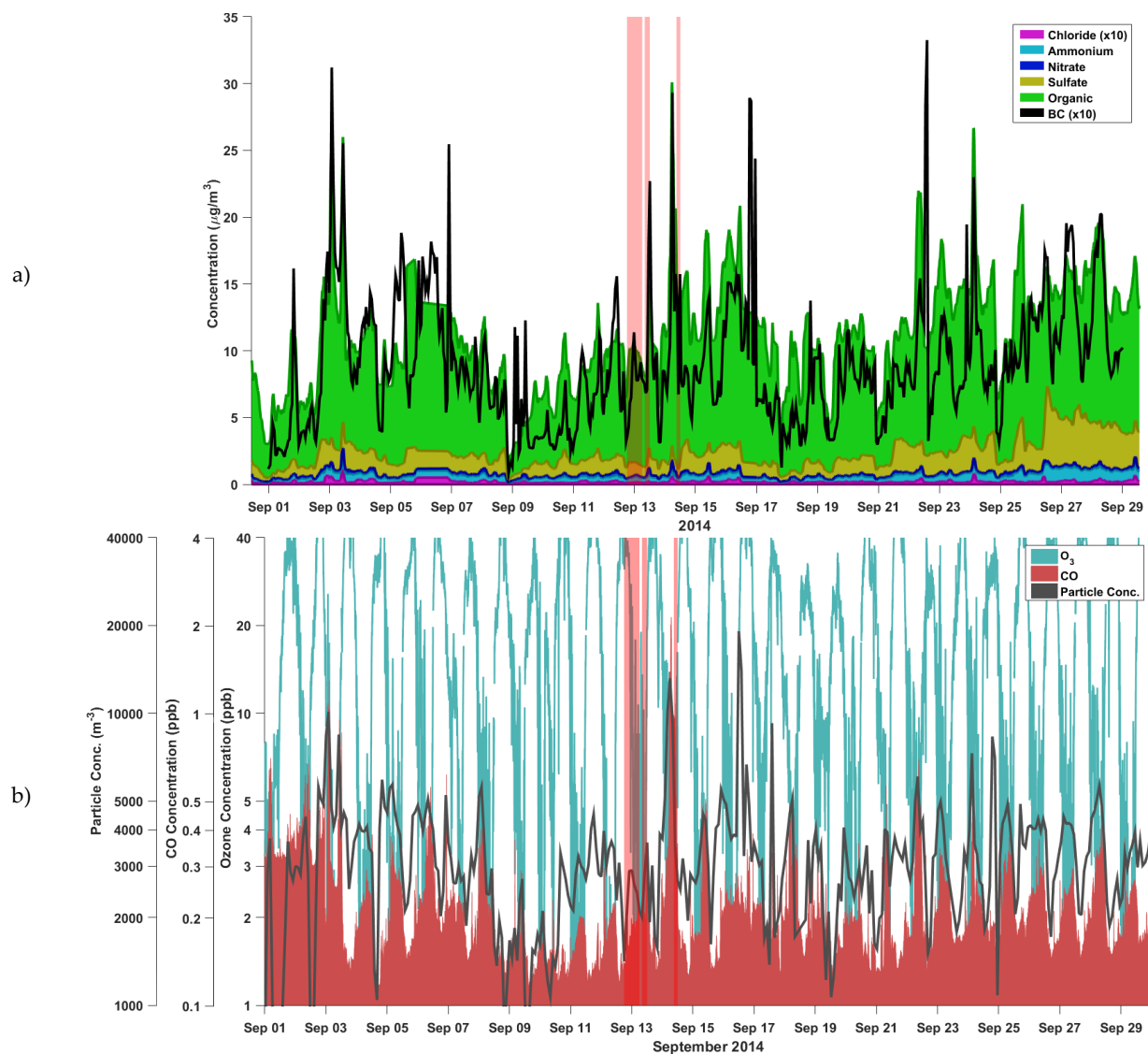
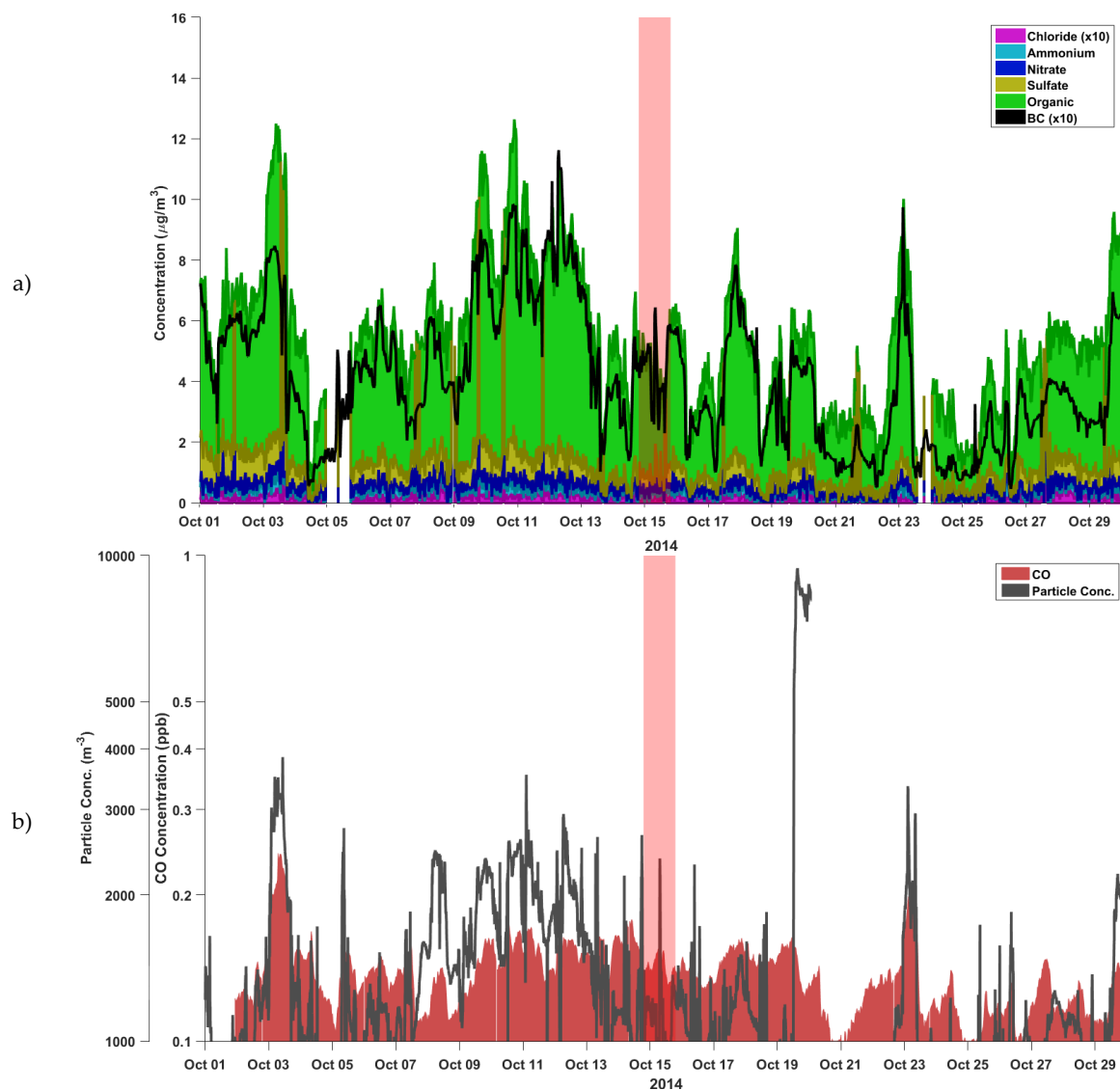


Figure S1. 72 hour HYSPLIT back trajectories starting at 500, 1000, and 1500 m Above Ground Level (AGL) for sites a) ATTO, b) ZF2, and c) T3.

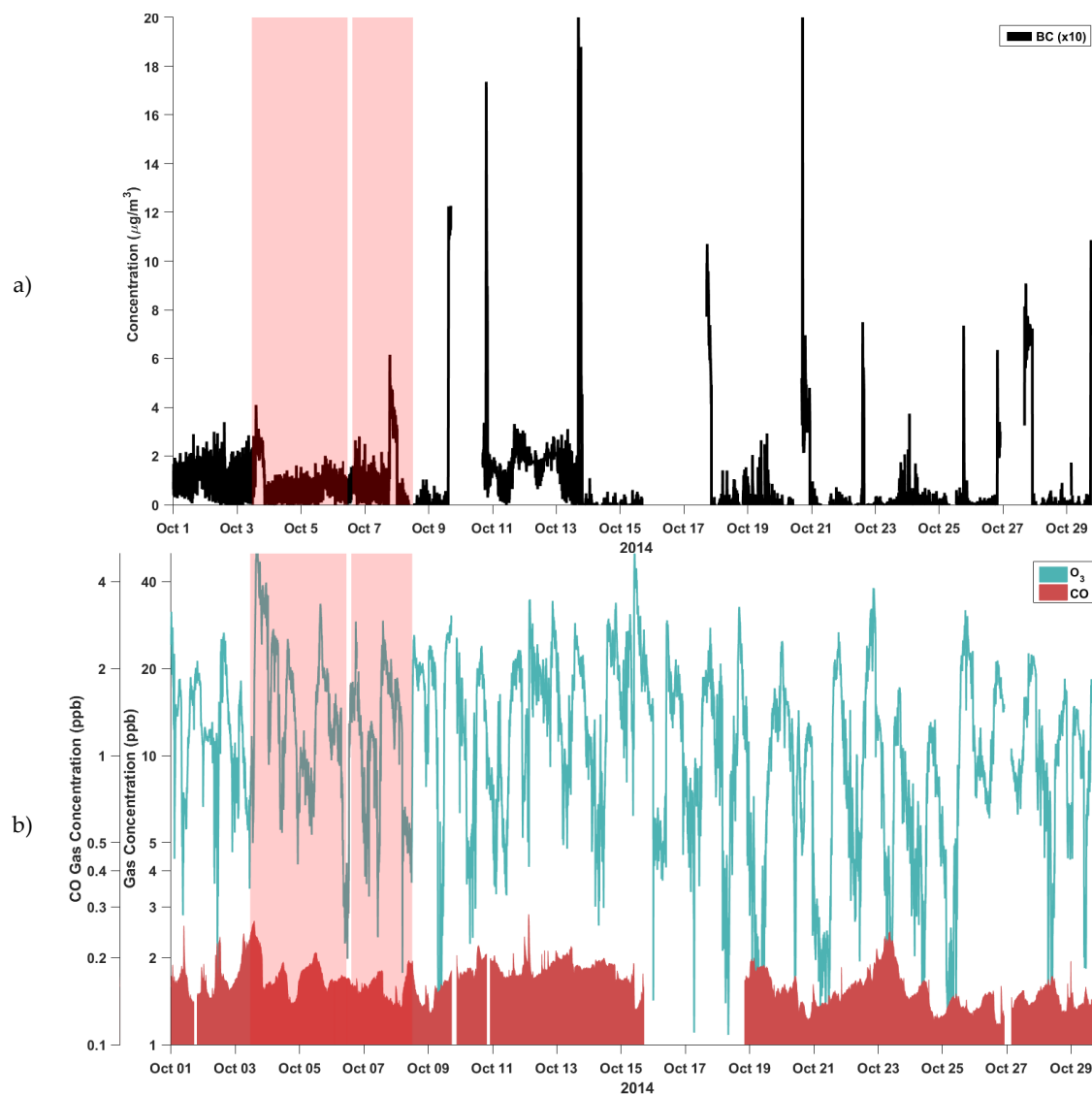
1
2



3 **Figure S2.** a) AMS and BC and b) Ozone, CO, and particle concentration time series for the month of September 2014 for the T3 Site. Light red bands represent
 4 sample collection periods. From right to left: 12/Sept 18:00 – 6:00, 13/Sept 8:00 – 12:00, 14/Sept 9:00 – 12:00



5 **Figure S3.** a) AMS and BC and b) CO and particle concentration time series for the month of October 2014 for the ATTO Site. The vertical light red band
6 represents the sample collection period from 14/Oct 19:00 – 15/Oct 19:00



7 **Figure S4.** a) BC and b) Ozone and CO time series for the month of October 2014 for the ZF2 Site. Vertical light red bands represent sample collection periods.
 8 From right to left: 3/Oct 11:00 – 6/Oct 11:00 and 6/Oct 14:00 – 8/Oct 12:00.